TECHNISCHE UNIVERSITÄT WIEN

ACIN AUTOMATION & CONTROL INSTITUTE INSTITUT FÜR AUTOMATISIERUNGS- & REGELUNGSTECHNIK

Adaptive Optics for Small Telescope Systems

DIPLOMARBEIT

Ausgeführt zum Zwecke der Erlangung des akademischen Grades eines
Diplom-Ingenieurs (Dipl.-Ing.)

unter der Leitung von

Univ.-Prof. Dr.sc.techn. Georg Schitter
DI Andreas Sinn

eingereicht an der

Technischen Universität Wien
Fakultät für Elektrotechnik und Informationstechnik
Institut für Automatisierungs- und Regelungstechnik

von

Jakob Maislinger
Matrikelnummer: 01527150

Wien, im Dezember 2023

Advanced Mechatronic Systems Group
Gußhausstraße 27-29, A-1040 Wien, Internet: http://www.acin.tuwien.ac.at

Danksagung

An dieser Stelle möchte ich mich zuerst bei Prof. Schitter bedanken, für die Möglichkeit dieses interessante Thema in einem ausgezeichneten Forschungsumfeld zu bearbeiten. Zudem auch an das hervorragende Arbeitsumfeld und die Möglichkeit als Studienassistent mitzuwirken.

Besonders möchte ich auch bei meinem Betreuer Andreas Sinn bedanken, für die herausragende Unterstützung und den immer sehr hilfreichen Rat und Tat.

Bedanken möchte ich mich bei meinen Freunden und Kollegen, für eine super Zeit und gegenseitig erstklassigen Support.

Abschließend geht mein größter Dank an meine Eltern Artur und Helga, Großeltern und Bruder, die mir diesen ganzen Weg erst ermöglicht haben! Für die ganze Unterstützung und das Vertrauen. Danke!

Abstract

Small telescope systems are commonly used in various applications such as astronomy, Earth observation and free-space optical communication. All those applications are susceptible to atmospheric turbulences, which limit the achievable performance. AO is used for correcting atmospheric turbulences in reflective telescope systems, by measuring the wavefront distortions and compensating them with deformable mirrors, thus restoring clear and sharp images. AO systems are highly complex and therefore hardly used in small telescopes (< 0.5 m), but nevertheless enable significant improvements in imaging quality for this telescope class.

In this thesis an AO system designed for a small telescope system is implemented and evaluated. A combination of a dedicated tip-tilt compensation system together with a higher order AO system is used to maximize the disturbance rejection. To measure aberrations, a Quad Photo Diode (QPD) sensor and a Shack Hartmann wavefront sensor (WFS) are used. The tip-tilt compensation system is implemented with a Fast Steering Mirror (FSM) and a QPD. Using PID control a -3 dB closed loop bandwidth of 1.045 kHz is achieved. The higher order compensation system uses a WFS and a Deformable Mirror (DM). An Integral controller is implemented resulting in a closed loop bandwidth of 42.6 Hz. The two proposed subsystems are used standalone as well in two combinations to analyze the achievable performance. Furthermore, the influence of a fast tip-tilt compensation system on higher order aberrations is analyzed and the dynamics of the DM are evaluated.

The AO system is characterized using a custom-made optical turbulence generator (OTG) oriented at the measured disturbance spectrum of a typical LEO object tracklet. This provides a reproducible disturbance to characterize the performance of the individual compensation approaches. The wavefront error is recorded using the WFS. In comparison to the uncompensated case the QPD-FSM loop reduces the wavefront error by a factor of 6.02 and WFS-DM by 4.56. With both systems combined an error reduction by a factor 10.88 is achieved, resulting in a clear and stabilized spot on the camera.

Zusammenfassung

Kleine Spiegelteleskope werden häufig in verschiedenen Anwendungen wie Astronomie, Erdbeobachtungen und optische Kommunikation verwendet. Diese Anwendungen werden beeinflusst von atmospherischen Turbulenzen, wodurch die Leistungsfähigkeit beschränkt ist. Adaptive Optik (AO) Systeme werden benutzt um atmospherische Turbulenzen in Spiegelteleskopen zu kompensieren. Die verzerrte Wellenfront wird dabei gemessen und mithilfe von verformbaren Spiegeln kompensiert. Dadurch werden klare und scharfe Bilder ermöglicht. AO-Systeme sind äußerst komplex und werden daher kaum in Teleskopen kleiner als 0.5 m eingesetzt. Dennoch lassen sich signifikante Verbesserungen damit erzielen.

In dieser Arbeit wird ein AO-System für ein kleines Teleskopsystem implementiert und getestet. Es wird ein System zur Tip-Tilt Kompensation mit einer für Störungen höhere Ordnungen kombiniert, um die Störunterdrückung zu maximieren. Zur Messung der Wellenfrontstörungen wird eine 4-Quadrantenphotodiode (QPD) und ein Shack Hartmann Wellenfrontsensor (WFS) verwendet. Zur Kompensation der Störung kommt ein schneller Kippspiegel (FSM) und ein verformbarer Spiegel (DM) zum Einsatz. Für QPD und FSM wird eine PID-Regelung implementiert und für WFS und DM eine Integral-Regelung. Die FSM Regelung erreicht eine -3 dB Bandbreite des geschlossenen Regelkreis von 1.045 kHz, die DM Regelung 42.6 Hz. Die Regelungen werden einzeln sowie in Kombination getestet. Darüber hinaus wird der Einfluss einer Tip-Tilt Kompensation auf Störungen höhere Ordnungen untersucht und die Dynamik des DM analysiert.

Das AO System wird mithilfe eines eigens gefertigten optischen Turbulenzengenerator (OTG) evaluiert, welcher das Störspekrum eines typischen LEO-Objekt-Tracklets nachbildet. Dies hat den Vorteil einer gleichen reproduzierbaren Störgröße, anhand welcher unterschiedliche Kompensationsstrategien charakterisiert werden können. Der resultierende Wellenfrontfehler wird mit dem WFS aufgezeichnet. Die DM Regelung verbessert den Wellenfrontfehler um einen Faktor von 4.56 und die FSM Regelung um 6.02. Mit beiden Regelungen kombiniert wird eine Reduktion von 10.88 erreicht, was zu einer deutlich besseren und ruhigeren Abbildung auf der Kamera führt.

Contents

List of Figures

List of Tables

CHAPTER 1

Introduction

1.1 Background and Motivation

Small telescopes are used in applications such as astronomy, Earth observation and optical communication. In these applications atmospheric turbulences lead to optical aberrations that limit the achievable performance. Adaptive optics (AO) is used as a versatile technology to correct such optical aberrations [4]. AO enables high resolution images close to the diffraction limit of the optical system or ensures a high communication bandwidth. An example for that is shown in Figure 1.1. The disadvantage of an AO systems is, that it is highly complex, expensive and therefore, typically only applicable in large telescope systems. Nevertheless, significant improvements can also be achieved in small telescope systems. [5, 2, 6]

The approach of AO consists of measuring and correcting optical aberrations. Atmospheric turbulence introduces optical aberration to the received light of telescope systems. Furthermore, wind-shake, tracking errors, vibrations and other environmental influence factors (e.g. temperature, gravity) reduce the imaging quality further. The measurement of these aberrations is accomplished by measuring the received wavefront with wavefront sensors. The correction of the deformed wavefront is typically achieved with active deformable mirrors (DMs). This process of measuring and correcting a wavefront is wrapped into a control loop so that the observed wavefront is always kept flat [7]. Figure 1.2 shows a simple schematic overview of observing an object through a telescope with AO.

The measured wavefront can be decomposed and represented as modes, commonly used are Zernike modes. The number of Zernike modes that are compensated for determines the complexity of the AO system [8]. Simple systems may only compensate for tip-tilt aberrations, while more complex systems also compensate for higher order modes like

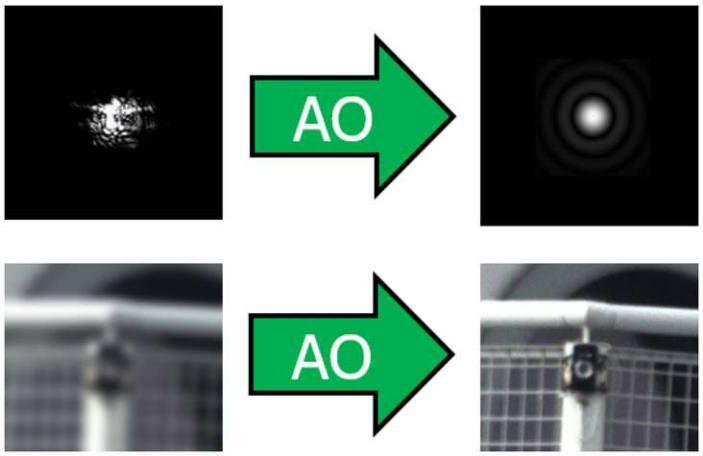

Figure 1.1: Example images without (left) and with (right) adaptive optics compensation.

astigmatism, coma, spherical aberration, etc. [7]. Because the lower order modes are the most dominant ones in atmospheric turbulences and the simpler ones to compensate for, a common approach is to divide the AO system into different stages, each targeting a specific set of aberrations [9]. The first stage targets lower order modes and therefore, uses DMs with fewer actuators. This leads to the advantage of cheaper and less complex mirrors with a higher range of motion and faster actuation. A prominent example is a fast steering mirror (FSM) which only compensates for tip and tilt. For higher order modes a more complex DM is needed which adjusts its surface accordingly [10]. This breakdown can also be applied for measuring wavefronts. A simple quad-photo diode can measure global tip-tilt modes fast and accuratly, while higher order modes need a more sophisticated approach like a Shack-Hartman wavefront sensor [11].

For large reflective telescopes, which are typically custom-made single unit projects, the cost of production is extremely high and an AO system of high complexity and accuracy is not the driving cost factor. In addition, larger telescopes are even more susceptible to atmospheric aberrations. However, this does not extend to small telescope systems with a diameter below 0.5 m. In this case the driving cost factor is indeed very dependent on the complexity of the adaptive optics system. Furthermore, the optimal tradeoff in correction performance (e.g. remaining RMS wavefront error (WFE), Strehl Ratio) and complexity (number of sensors, actuators, control loops) is not well studied yet for small telescope systems, as there only exist a few research papers [5, 2, 6]. A deeper understanding of the interaction between performance and complexity is therefore, a desired goal of scientific research.

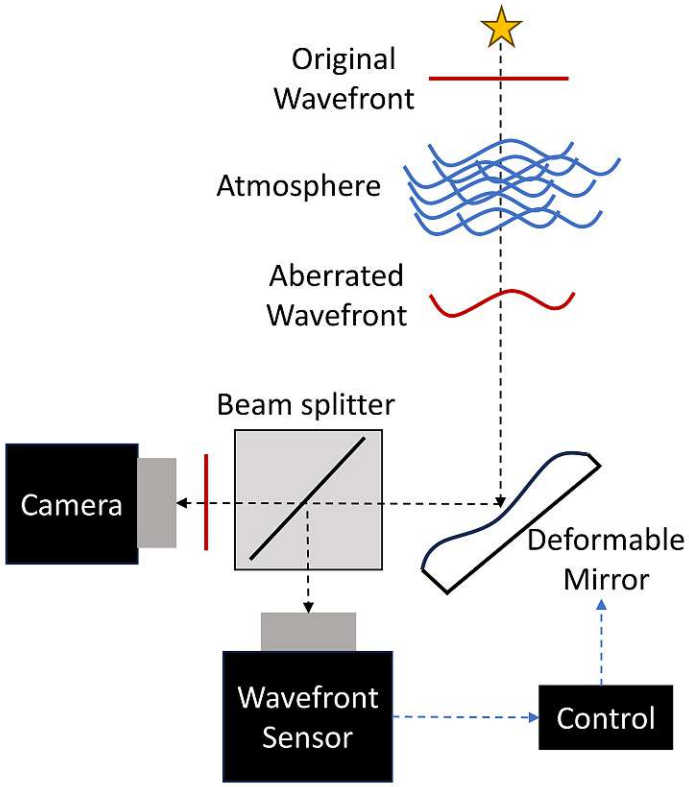

Figure 1.2: Schematic overview of observing an object with adaptive optics.

1.2 Research Challenges and Goals

In this thesis an AO system with tip-tilt and higher order compensation is designed, implemented and evaluated for an application in a small telescope system. Different compensation approaches such as tip-tilt compensation, higher order compensation and their possible combination shall be evaluated. One focus is to maximize the disturbance rejection of the implemented system, to enable a high quality imaging system. A method to introduce a reproducible disturbance for evaluation of the implemented strategies is required and shall be developed within this thesis. The key goals are:

- Design and implement an adaptive optics system design oriented at the requirements of small telescope systems with an aperture below 0.5 m.
- System identification, controller design and evaluation of single stage compensation as well as combinations of compensation approaches.
- Simulation of atmospheric turbulences to enable a reproducible disturbance for characterization of different compensation approaches.
- Experiments to characterize the performance of the AO system.

1.3 Thesis Outline

Chapter 2 (**State of the Art**) starts with an overview on current research of AO systems in small telescopes. It proceeds to describe compensation approaches such as woofer-tweeter systems and explains the different components used in AO systems. Furthermore, it characterizes atmospheric aberrations and describes ways on how to recreate them in optical turbulence generators.

Chapter 3 (**Optical Design**) is all about the creation and implementation of the optical design used and divides the AO system into two main subsystems.

Chapter 4 (**Control Systems**) develops the control systems for the two optical subsystems, with the process being subdivided into system identification, controller design and controller evaluation. Following this, a communication between the two subsystems is established.

Chapter 5 (**Optical Turbulence Generators**) examines methods for replicating atmospheric disturbances and characterizes the final implemented optical turbulence generator.

In Chapter 6 (**Experiments**) the performance of the AO system is evaluated with the implemented optical turbulence generator through various experiments.

Chapter 7 (**Conclusion and Outlook**), summarizes the results and gives an outlook for further research and improvements.

CHAPTER 2

State of the Art

The inventor of AO is considered to be Horace Babcock. He published the paper "The Possibility of Compensating Astronomical Seeing" in 1953, which states the first possible approach of compensating atmospheric turbulences in reflective telescopes by using a DM and wavefront detection [4]. It took around 30 years but with projects like "Come On" in 1989, this concept could be successfully proved in real setups [12]. Nowadays AO systems are used in the largest earth stationed reflective telescopes like the Subaru Telescope, Keck 1/2 and the Large Binocular Telescope to improve image quality [13, 14, 15]. The principle of AO is not limited to large reflective telescopes and can also be used in small telescope systems [6].

2.1 Adaptive Optics in Small Telescopes

AO can significantly improve the image quality of observations in telescope systems. However, due to its complexity and cost, very few attempts were made to implement such systems in small telescopes with a diameter below 0.5 meters. In a study published in 2015, a compact AO design for an 16" (406.4mm) telescope was implemented (Figure 2.1). In this design a DM with 21 actuators and a wavefront sensor with 10x10 subapertures each having a detection array of 30x30 pixels was used. It successfully demonstrated a reduction of the spectral energy in the temporal variation of the Full Width Half Maximum (FWHM). This study emphasizes the viability and improvement in image quality of an adaptive optics system in small telescope systems [1].

Low order optical aberrations dominate the wavefront error of small telescopes, with tip-tilt being the largest single contributor. Tip-tilt errors build up due to tracking error, bad alignment or atmospheric aberrations and make up most of the wavefront error in good seeing conditions. In this study [5] published in 2008 an AO system was

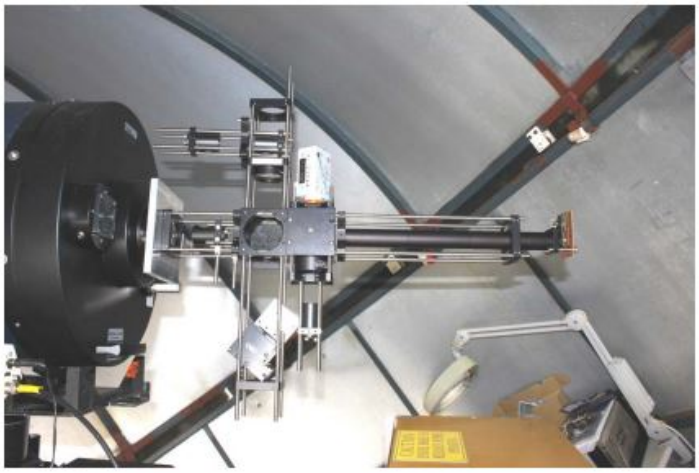

Figure 2.1: Compact Adaptive optics system attached to a 16" Meade LX200ACF Telescope [1].

tested on 25 to 36 cm diameter telescopes using a DM and Shack-Hartmann wavefront sensor. The main source of wavefront error was found to be tip-tilt due to tracking error and not perfect alignment as well as astigmatism in consequence of the telescope design. Higher order atmospheric aberrations were found to have an insignificant influence on the wavefront error. The on sky tests were conducted on a natural star of magnitude 2.21 in good atmospheric conditions.

In suboptimal atmospheric conditions higher order modes are more prominent. Such conditions are commonly encountered during tracking of satellites, optical communication as well as by amateur astronomers due to use of not ideal locations. Therefore, it can be advantageous to employ a compensation strategy beyond tip-tilt up to higher order modes. A study from 2018 was done on an 11" (279.4 mm) telescope by using a multi-actuator adaptive lens due to its simpler design than a DM. The on sky tests were carried out in relatively bad seeing conditions observing the star Vega. The results show significantly improvements with tip-tilt compensation and even further improvements with additional compensation of higher modes. Figure 2.2 shows the results in two plots [2].

Another use case for AO in small telescope systems is optical communication. In free-space optical (FSO) satellite communication atmospheric turbulences interfere with the data transmission. Especially in reflective FSO communication, where the laser beam has to pass the atmosphere twice [16]. Tip-tilt aberrations contribute to around 80% of the total wavefront error and therefore, high-performance tip-tilt compensation systems are used for compensation [17]. However, for this use case the need for compensating higher-order modes is not given as it does not involve any imaging and is not improving the coupling of the light into optical fibers for further data analysis.

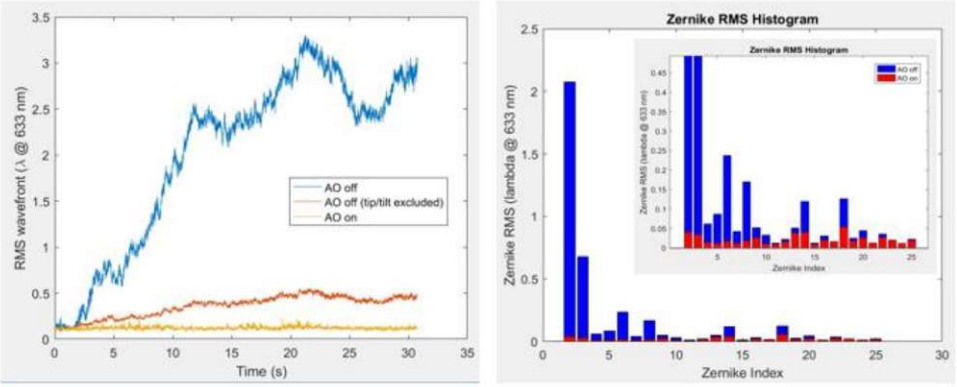

Figure 2.2: Measured RMS wavefront error of Vega with different controls (left); Zernike coefficient RMS values over 30 s with AO on and off excluding tip-tilt (right) [2].

2.2 Woofer-Tweeter Systems

The fundamental process of AO is the detection and compensation of wavefront aberrations. In reflective telescopes typically a DM is used for the compensation part. To compensate all atmospheric aberrations, the DM needs to have the ability to adjust for large amplitudes in high spatial resolution. This characteristic is very difficult to combine in one DM and therefore, the workload is often times split up into two DMs, a woofer and a tweeter [18]. The terminology is inspired from two speaker audio-systems, but instead of temporal frequencies being the choice of separation, spatial frequencies are used. The woofer compensates for large stroke low-order aberrations. The tweeter compensates for low stroke high-order aberrations [19]. This is reasonable because in atmospheric aberrations most power is found in low spatial frequencies [20]. Therefore, larger stroke ranges are needed for low-order wavefront aberrations and smaller strokes are sufficient for higher-order spatial frequencies [21]. This also defines the physical order of the two DMs with the woofer doing the first heavy step and the tweeter later doing the finer adjustments [22]. Figure 2.3 shows the sequence of such a compensation process.

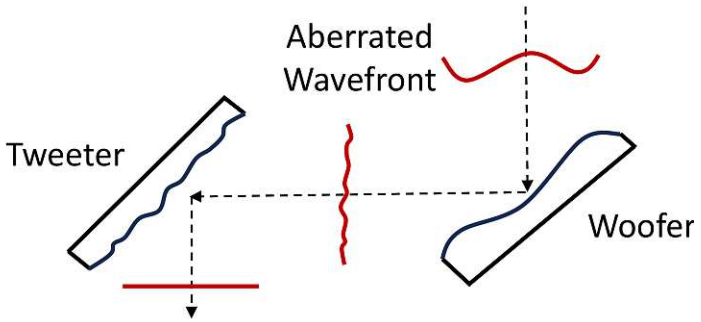

Figure 2.3: Woofer and tweeter system showing the two step process of compensating an aberrated wavefront.

Woofer and tweeter systems are a numerously tested principle in reflective telescopes.

Many variants exist taking advantage of the different kinds of DMs. They differ in number of actuators, actuator technologies, size and many other features [22]. The simplest structure for a woofer tweeter system is to split up the workload into a tip-tilt mirror and a DM. The tip-tilt mirror corresponds to the woofer, compensating the lowest order tip-tilt modes. Large strokes are needed for these tip-tilt modes. The remaining wavefront error is compensated by the DM [23]. For this task less stroke range is needed, but with higher spatial resolution. A possible consequence of this separation in the spatial frequency domain is, that it can also cause a separation in the temporal frequency domain. The application frequency of the two mirror systems can differ due to the difference in complexity. FSM, which can adjust in tip-tilt, have a simpler structure than DMs and are able to operate up to high frequencies. On the other hand DMs are often limited to lower frequencies. This creates an additional separation in the temporal frequency domain and therefore, different bandwidths are covered by the two mirror systems. In an AO system this second separation also has to be considered in the closed loop controller design as well as in the evaluation of the combined system.

The separation of the spatial frequency domain can also be applied to the measurement of wavefront aberrations. Tip-tilt modes for example can be detected with a quad-photo diode. For higher modes a more sophisticated approach like a Shack-Hartmann wavefront sensor is needed. The difficult part results from using the measured information and distributing it to individual mirrors without any undesired crosstalk or actuator saturation. For this reason different control strategies can be used. In [24], the main methods of control strategies have been listed: Zernike mode decomposition algorithm [25, 26, 27], Fourier mode decomposition algorithm [28], wavelet mode decomposition algorithm [29], Lagrange multiplier damped least-squares algorithms [30, 31, 32], and direct slope based correction algorithm [33, 34, 35].

2.3 Wavefront Sensors

2.3.1 Quad Photo Diode

The QPD is a sensor used in AO to measure tip-tilt aberrations. It consists of four photodiodes that each measure the intensity of incident light and generate a corresponding electrical signal. The photodiodes are arranged in a square with minimal spacing between each other. To measure tip-tilt deviations, the beam of an optical system is focused onto the QPD. Figure 2.4 shows the basic structure.

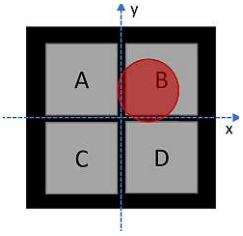

Figure 2.4: QPD sensor with 4 photodiodes and a focused laser beam.

Movements of the beam in x and y direction can be precisely detected by using the electrical signals of each photodiode. The deviations are calculated by

$$U_x = \frac{(U_B + U_D) - (U_A + U_C)}{(U_A + U_B + U_C + U_D)} \tag{2.1}$$

and

$$U_y = \frac{(U_A + U_B) - (U_C + U_D)}{(U_A + U_B + U_C + U_D)}, \tag{2.2}$$

where U_A, U_B U_C and U_D are the voltages of the single photodiodes [36]. The corresponding characteristic curve of U_x and U_y is shown in Figure 2.5 by the QPD output. The desired operation range is the linear region in the middle of the curve. In this region the beam covers some photodiodes more than the others resulting in valid x and y deviation information. Beyond this region the beam starts to move off some of the photodiodes and as a result the curve has a maximum. If the light beam starts to entirely move off the detection area the voltage starts to drop. The sensitivity of the linear section can be increased by decreasing the beam size. As a consequence the measurement range also decreases and the limiting factor is the spacing between the photodiodes. The beam diameter is recommended to be atleast 10 times the gap width.

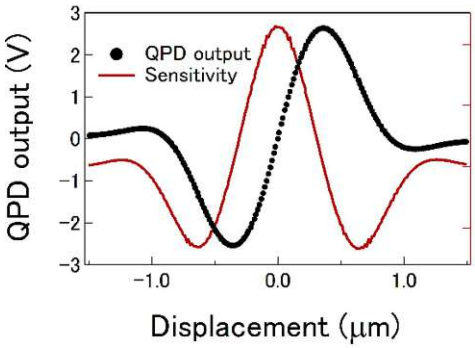

Figure 2.5: QPD characteristic curve by QPD output [3].

2.3.2 Shack-Hartman Wavefront Sensor

In AO systems wavefront sensors are required to provide real-time information of the entire wavefront of the incoming light. A frequently used sensor is the Shack-Hartman wavefront sensor. It divides the wavefront into an array of individual measurements that give feedback about the local slope of the wavefront. This is achieved by using a lenslet array with every subaperture having the same focal length. Each lenslet focuses the light on to a detection layer which consists of a CCD/CMOS array. The detection layer is placed exactly at the focal length of the lenslet. The detected position of the centroid gives the slope information about the wavefront. This data can be used to

reconstruct the shape of the wavefront. Figure 2.6 shows the working principle of a Shack-Hartman wavefront sensor.

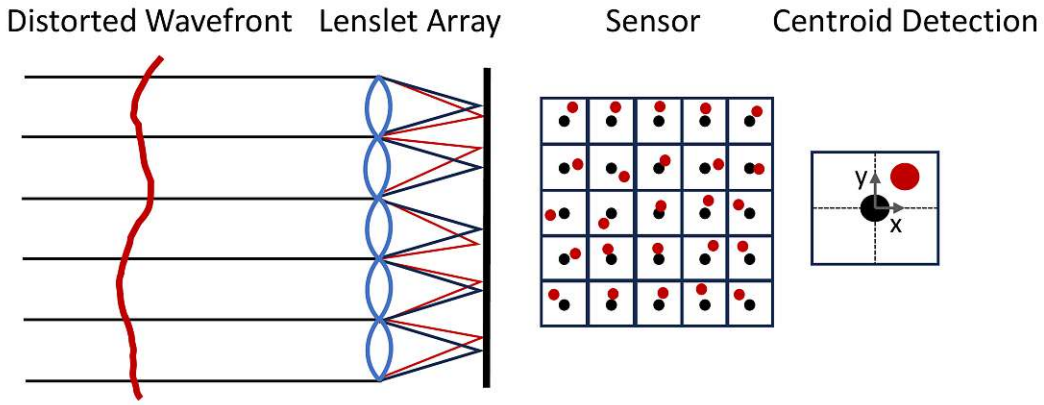

Figure 2.6: Principle of a Shack-Hartman wavefront sensor.

Two main methods are commonly used to represent wavefront aberrations, zonal and modal. The zonal representation divides the wavefront into discrete zones and displays the values associated with each subregion. It is a straightforward, simple approach that is beneficial for high order wavefront aberrations. The modal representation divides the wavefront into a set of orthogonal polynomials called "modes". The most popular set of polynomials for wavefront aberrations are the Zernike polynomials. The Zernike modes represent distinct patterns like tip, tilt, defocus, astigmatism, coma, trefoil and so on. This approach is especially beneficial if the wavefront consist of low order aberrations. In atmospheric aberrations most dominant modes are the lower order aberrations, consequently using Zernike polynomials is a suitable and convenient approach [37]. Figure 2.7 shows the two wavefront representations.

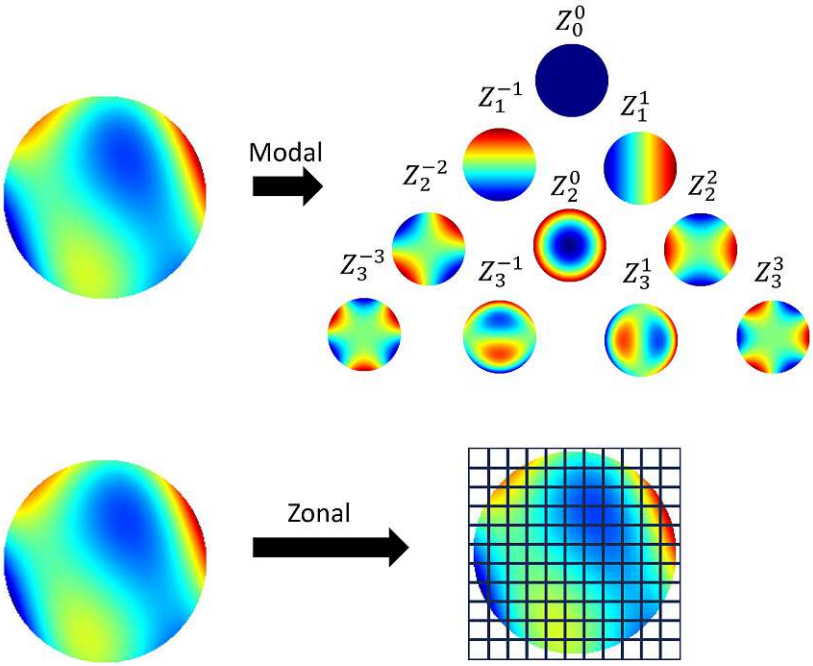

Figure 2.7: Modal and zonal wavefront representations.

The mathematical formulation and ordering for Zernike modes by Robert J. Noll is given in Equations 2.3, 2.4 and 2.5. The overall wavefront error is the sum of every Zernike polynomial Z_n^m times the coefficient c_n^m that describes the magnitude of each specific mode. Every Zernike mode polynomial consists of a normalization term, a radial function $R_n^m(r)$ and an angular term. The resulting equations for the first modes are listed as examples. The radius r corresponds to the normalization $\frac{\rho}{R}$ with R being the radius of the specific aperture [8].

$$W(r,\theta) = \sum_{n}^{N} \sum_{m=0}^{n} c_n^m Z_n^m(r,\theta) \tag{2.3}$$

$$\begin{aligned} Z_n^m(r,\theta) &= \sqrt{n+1} R_n^m(r) \sqrt{2} cos(m\theta) && \text{m} \neq 0 \\ Z_n^{-m}(r,\theta) &= \sqrt{n+1} R_n^m(r) \sqrt{2} sin(m\theta) && \text{m} \neq 0 \\ Z_n^0(r,\theta) &= \sqrt{n+1} R_n^0(r) && \text{m} = 0 \end{aligned} \tag{2.4}$$

$$\begin{aligned} Z_0^0(r) &= 1 && \text{Piston} \\ Z_1^{-1}(r) &= 2r sin(\theta) && \text{Y-Tilt} \\ Z_1^1(r) &= 2r cos(\theta) && \text{Z-Tilt} \\ Z_2^{-2}(r) &= \sqrt{6} r^2 sin(2\theta) && \text{Oblique Astigmatism} \\ Z_2^0(r) &= \sqrt{3}(2r^2 - 1) && \text{Defocus} \\ Z_2^2(r) &= \sqrt{6} r^2 cos(2\theta) && \text{Vertical Astigmatism} \\ &\ldots \end{aligned} \tag{2.5}$$

2.4 Wavefront Correctors

2.4.1 Fast Steering Mirror

A FSM is an opto-mechatronic device that adjusts a plane or flat mirror in tip-tilt. It consists of a compact design with high speed and precision capabilities. Different actuation principles like piezo, voice coil or reluctance actuation can be used [38]. The FSM allows for fast, precise and large direction changes of an optical beam, commonly needed for tip-tilt compensation in AO. FSMs are typically the first stage of stabilizing and improving an optical beam. In special cases FSM and DMs are combined with the DM mounted on top of a tip-tilt stage [39].

A very common actuation technology are voice coil actuated FSMs, which use the Lorentz force to move the mirror surface in tip-tilt motions. Lorentz force actuated FSMs have a larger angular range than piezo actuated FSMs but achieve less system bandwidth with up to around 1 kHz [38]. The FSM design is typically divided into two axes that can be independently controlled in case of a decoupled design. This allows for single input and single output (SISO) control designs. The typical structure of a FSM with voice coil actuation is shown in Figure 2.8.

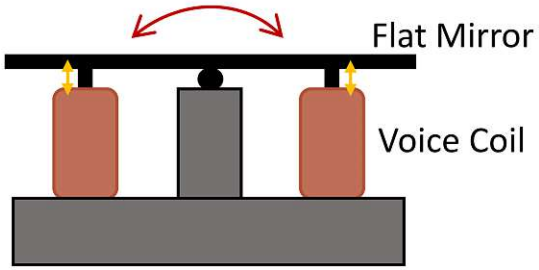

Figure 2.8: Schematic and simple representation of a FSM.

2.4.2 Deformable Mirror

Mirrors that can be modified into different shapes are called DMs. In AO the deformation of the mirror shape is used to compensate for wavefront aberrations. There are many kinds of DMs, depending on the special requirements for the optical system. DMs can be continuous like membrane mirrors or bimorph mirrors. They can be continuous with discrete actuators below or to the sides of the surface. They can also be segmented in areas with discrete actuators for each surface. Discrete actuators can also be stacked in case of the need of larger strokes. DMs also differ in actuation technologies. There are piezoelectric or electrostrictive actuators that change their shape in an electric field; voice-coil actuators, that use the Lorentz force; MEMS mirrors with electrostatic activation or so on. In general, the need for correcting atmospheric aberrations drives DMs towards increasing actuator numbers, miniaturization, low operating voltages, position accuracy and low hysteresis. The specifications are also very dependent on the use case. They can have a few actuators up to 30000 for 40 m class telescopes [40].

Typical stroke ranges are from 3 µm up to around 5 mm for fewer actuated DMs [40, 41]. In Figure 2.9 an exemplary technical concept of a DM is shown, using a continuous reflective surface deformed by voice coil actuators.

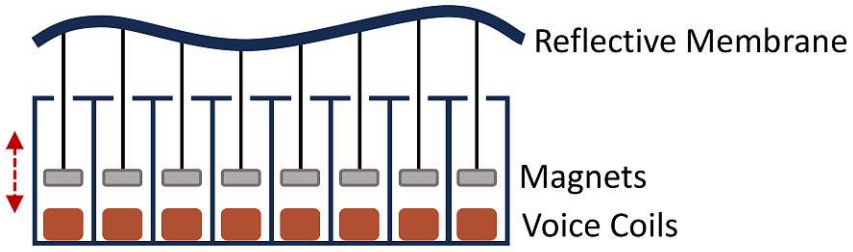

Figure 2.9: Technical concept of a voice coil actuated and continuous reflective surface DM.

2.5 Atmospheric Aberrations

The quality of all Earth-bound observations and communication links is influenced by distortions in light due to earth's atmosphere. Small changes in temperature result in different wind speeds or can also change the density of the atmosphere which then leads to different refraction indexes. These effects and others accumulate and cause aberrations in the final observation [42]. In AO it is important to have a deeper understanding of the characteristics of such aberrations in order to select and implement the most effective compensation strategy.

Long exposure observations of bright objects like stars, planets or satellites show a typical noise characteristic that can be analyzed and modeled. One widely accepted model which summarizes turbulent phenomenas in the atmosphere is the Kolmogorov model [42]. It divides the atmosphere into large regions (outer scale) down to small regions (inner scale) and defines that first energy is added to the larger regions and then breaks down to the small regions. All of these regions influence the light propagation. This model can be used to describe the power spectrum of atmospheric turbulences. The shape of the curve is proportional to the power of -11/3 at higher frequencies and to the power of -2/3 at lower frequencies [42]. Another key value for AO systems is the Greenwood frequency which is a measure for the rate of change of the Kolmogorov turbulences and defines the closed loop bandwidth needed for compensation [43]. As a rule of thumb the closed loop bandwidth should be 10 times the value of the Greenwood frequency. In Figure 2.10 the measured single side power spectral density of a tip-tilt measurement of the LEO object SL16RB is shown [44]. The model fits well to the data and shows a typical bandwidth of atmospheric aberrations up to around 200 Hz. Most power is contained in lower frequencies indicating the need for good compensation in that frequency range.

Atmospheric aberrations cause different effects like beam wandering, intensity variation (scintillation) and higher order wavefront variations. Therefore, it is important to

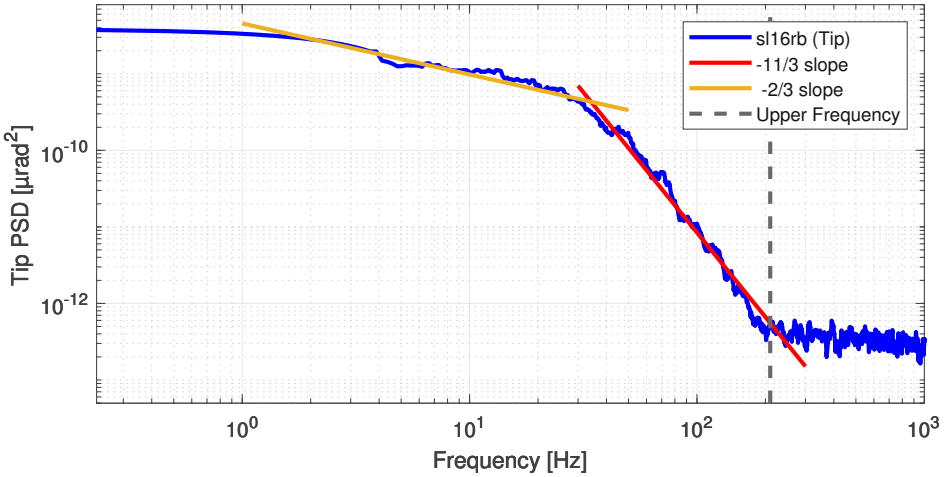

Figure 2.10: QPD tilt measurement of LEO object SL16RB and the distinct Kolmogorov model slopes.

analyze the distribution of aberrations across different Zernike modes, especially for small telescope systems. The Kolmogorov model allows to calculate how much residual wavefront variance is left after the compensation of specific number of modes. Besides these values the wavefront variance is also influenced by the aperture diameter of the telescope and the Fried's coherence length. The Fried's coherence length also called Fried's parameter r_0 quantifies the strength of atmospheric turbulence in meter [45]. Its length defines the distance at which the light remains coherent before being distorted by atmospheric turbulence. Equation 2.6 lists the wavefront variances for specific number of compensated modes:

$$
\begin{aligned}
\sigma^2 &= 1.030(\frac{D}{r_0})^{5/3} && \text{0 modes removed} \\
\sigma^2 &= 0.582(\frac{D}{r_0})^{5/3} && \text{1 mode removed (tilt axis 1)} \\
\sigma^2 &= 0.134(\frac{D}{r_0})^{5/3} && \text{2 modes removed(tilt axis 1+2)} \\
\sigma^2 &= 0.111(\frac{D}{r_0})^{5/3} && \text{3 modes removed} \\
\sigma^2 &= 0.088(\frac{D}{r_0})^{5/3} && \text{4 modes removed} \\
&\dots \\
\sigma^2 &= 0.2944N^{-\sqrt{3}/2}(\frac{D}{r_0})^{5/3} && \text{N modes removed,}
\end{aligned}
\tag{2.6}
$$

σ^2 is the WFE variance, r_0 the Fried's parameter and D the aperture diameter of the telescope. The wavefront variances drop significantly with rising number of modes compensated for. By removing tip-tilt modes the variance can already be minimized by a large margin in most cases. The ratio $\frac{D}{r_0}$, aperture diameter of the telescope to Fried's

coherence length, takes substantial influence in how large the wavefront variance is. The Fried parameter varies between approximately 5 cm for poor seeing conditions up to around 20 cm for good seeing conditions. Telescope apertures that match this length perceive minimal higher order atmospheric aberrations. However, telescope apertures that exceed this value experience increasing levels of atmospheric aberrations. As a result AO in small telescope systems is especially beneficial in poor seeing conditions and for low order aberrations.

The quality of an imaging system can be defined with the Strehl ratio by

$$S = e^{-\sigma^2}, \tag{2.7}$$

where σ^2 is the variance of the wavefront error [46, 47]. The Strehl ratio is expressed as a value ranging from 0 to 1, with 1 being a perfect diffraction limited system without any aberrations. The improvement in the Strehl ratio of an AO system, influenced by the ratio $\frac{D}{r_0}$ and different number of Zernike modes, can be calculated and plotted in Figure 2.11 [48]. This figure points out that for low ratios of $\frac{D}{r_0}$ the main improvement of image quality is achieved by the compensation of tip-tilt modes. Small telescopes with a diameter below 0.5 m have a dominant tip-tilt error, consequently compensating tip-tilt aberrations well reduces most of the wavefront error. But around 20 % WFE remains with a perfect tip-tilt compensation, due to the WFE error consisting of higher order aberrations. For further increase in image quality it makes sense to try higher order AO compensation for the remaining 20 percent.

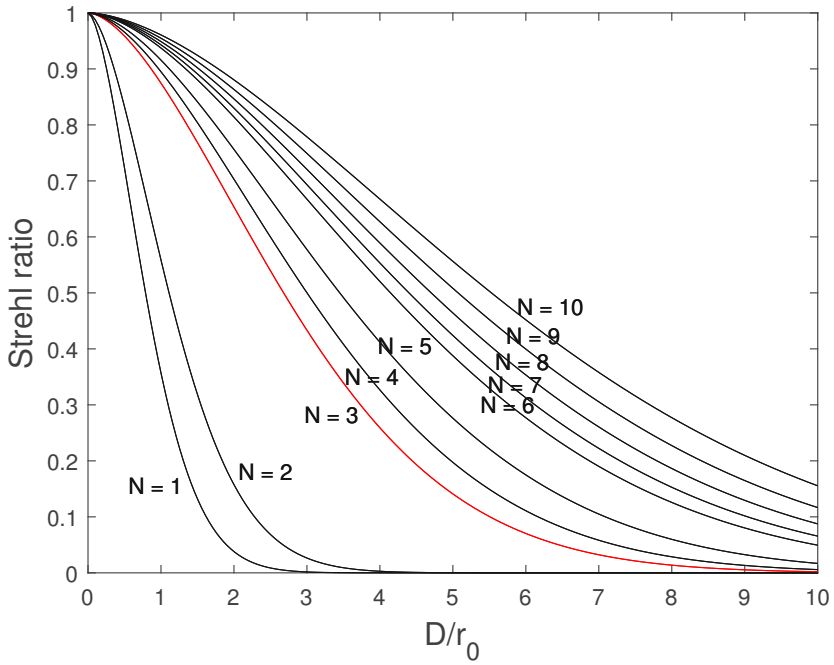

Figure 2.11: Theoretical Strehl ratio along the ratio $\frac{D}{r_0}$ with different number of modes (N) compensated for.

2.6 Optical Turbulence Generators

Optical turbulence generators are used to mimic atmospheric aberrations. They allow evaluation of AO systems in a controlled and reproducible environment and in some cases without the use of the target telescope system. Therefore, telescope time can be minimized, and the setup can be tested in a laboratory environment, which makes the optimization of the adaptive setup much more convenient. A high quality laser beam is required as reference for calibration and evaluation of the AO system. The optical turbulence generator is then incorporated into the beam path and a specific atmospheric aberrations profile is introduced. The challenging part of an optical turbulence generator is the exact recreation of a specific noise profile like the SL16RB measurement from the previous section.

There are many different types of noise generators like rotating static phase screens, dynamic reconfigurable phase screens or turbulent-fluid chambers [49]. Rotating static phase screens typically consist of a rotating disc with introduced distortions that alter the light beam which is passing through [50, 51, 52]. Examples for dynamic reconfigurable phase screens are liquid crystals that can modulate the light or DMs [53]. Turbulent-fluid chambers use hot air or other fluids to create physical turbulence in a confined space [54]. The difference in temperature of the fluids is crucial here for the creation of turbulent flow.

Rotating Static Phase Screens have the advantage of producing a specific and fixed noise profile that repeats itself after a full rotation. The time until the pattern repeats itself can be increased by adding multiple Static Phase Screens with different rotation speeds. It is a simple and compact way of introducing aberrations. By bending the phase screens tip-tilt aberrations are introduced, which is an important aspect in this thesis. The higher order modes are produced by altering the surface to add an optical path difference to the phase screen. This can be done by etching the surface of the phase screen or applying specific molds to plastic phase screens [49]. A cheap and simple solution is to apply standard hairspray to a glass plate. This leads to surprisingly accurate imitations of atmospheric turbulences [52].

2.7 Research questions

The state of the art took a closer look at AO systems in smaller telescopes. It described woofer-tweeter systems and gave examples for wavefront sensors such as QPD and Shack-Hartmann-sensor as well as wavefront compensators such as FSM and DM. It characterized atmospheric aberrations and explained how those can be artificially recreated with optical turbulence generators. With the gathered information four research questions are outlined:

Existing papers of AO in small telescopes have shown that compensation of higher order modes can have a positive impact on the performance. The exact impact is analyzed in Research Question 1:

> Research Question 1: How does the trade-off between correction performance and number of compensated modes affect the overall system's performance?

The next question takes a close look at the interaction between WFS and DM. It focuses on the dynamic behavior of the DM and questions if the dynamic behavior has to be taken into account in the control system design.

> Research Question 2: Is the dynamic behaviour of the DM observed at the wavefront sensor and therefore needs to be considered in the control system design?

The third question addresses if there is a connection between tip-tilt compensation and higher order modes.

> Research Question 3: How does the tip-tilt compensation affect higher-order aberrations and their compensation?

The last question examines whether tip-tilt and higher-order compensation can be achieved with independent controller designs.

> Research Question 4: Is it possible to sepearate the controller design of tip-tilt compensation and higher order compensation?

CHAPTER 3

AO System Design

Upon the insights obtained from previous research about small telescope systems as well as additional information from Chapter 3, this section deals with an optical design of an AO system for a small telescope system. The chapter starts with the optical system requirements and telescope specifications. Following this the optical design is introduced and the requirements for the subsystems are determined. At last, a closer look at the design of the optical subsystems is taken in order to satisfy the requirements.

3.1 Telescope and Optical Requirements

The AO system is designed for a 14" Schmidt-Cassegrain telescope. The telescope is mounted on an active vibration-isolated table that minimizes disturbances and which is also used as the foundation of the optical setup. For further research, the telescope is pointed towards a building with a distance of around 300 meters and with a possible mount for a retroreflector which can be used to create a 600-meter reflective free-space optical (R-FSO) communication link. This allows for testing the AO-system in a harsh urban environment. Additionally, for further research there is also the option to test the AO setup on an identical telescopes outdoors on stars. Therefore, the optical design is not designed for a specific task, but rather to get a general understanding of the interactions in higher order compensation systems and show the possible potential and flaws of such a system.

The light collected by the telescope with 355 mm diameter is collimated to a beam diameter of 10 mm. This reduction in beam size leads to a multiplication of the observed tip-tilt fluctuations (jitter) in the optical system by the inverse ratio. Accordingly, for the 14-inch telescope the observed jitter in the AO system is 355.6/10 greater than at the telescope entrance as shown in Figure 3.8. For an optimally tip-tilt-compensated

measurement and jitter free image a RMS value of 0.28 µrad was assumed at the telescope entrance. Therefore, the desired accuracy of the tip-tilt compensation needs to be <10 µrad RMS. Due to the atmospheric aberrations an entrance error of around 8 µrad RMS is expected, which leads to jitter in the optical system of around 300 µrad RMS. Consequently, the disturbance rejection of the implemented tip-tilt compensation needs to be larger than a factor of 30 for a jitter free image.

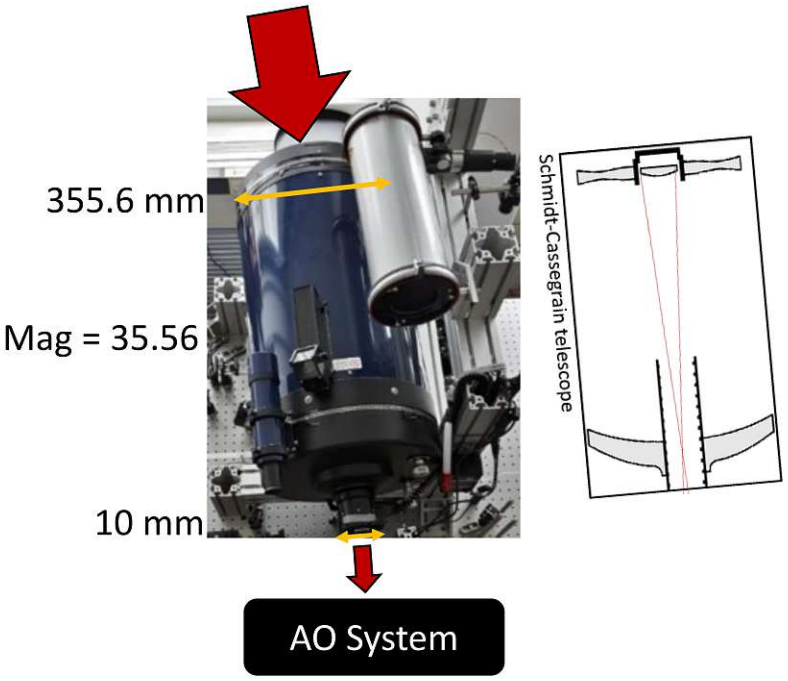

Figure 3.1: Overview and tip-tilt magnification by the 14-inch telescope.

The diameter of the telescope entrance allows for broad classification of the ratio D/r_0. The Fried parameter r_0 varies within the range of 5 cm for bad seeing conditions up to 20 cm for good seeing conditions as discussed in Chapter 2. This leads to a D/r_0 ratio range of 1.77 to 7.112 and as a result the optimal achievable tip-tilt compensation ranges from 70.7% to 3.0% of the total wavefront error according to Figure 2.11. The compensation needs to achieve a higher bandwidth than that of atmospheric turbulences, which has an upper frequency of around 200 Hz according to Figure 2.10.

3.2 Optical Setup

The goal is to create an optical design that combines tip-tilt compensation with higher-order compensation. To systematically test the system, a laser is implemented as a reference input to the optical system. For the tip-tilt compensation, a FSM Prototype (FSM3000) from micro-epsilon (Ortenburg, Germany) is used and for the compensation of higher order modes a DM (DM69) from Alpao (Montbonnot, France). Wavefront measurements will also be split up into two sensors, a QPD for the tip-tilt modes and a Shack-Hartmann wavefront sensor (HASO3 FAST) from Imagine Optic (Orsay,

France) for up to higher order modes. The light beam is split using 50/50 beam splitter and mirrors and lenses are utilized for the remaining connections and conjugate plane matching to complete the setup. Figure 3.2 shows the final setup in detail and Table 3.1 lists all used components.

The setup starts with a laser and lens L0 that collimates the laser beam. The collimation is verified by a Shear interferometer and the size of the beam is adjusted to a diameter of 1.3 cm using a variable aperture. To adjust the beam intensity a variable neutral density filter is added. The light beam is then aligned past the potential telescope input by a flip mirror, creating a considerable amount of distance before entering the AO system. This allows for the placement of the OTG to alter the beam and thus simulating the atmospheric turbulences. Before entering the AO system the laser beam is adjusted to 1 cm beam diameter with a second aperture. This aperture is placed exactly at the focal length of the next lens L1 which creates an optical relay with the same lens L1 again. As a consequence the FSM plane and Aperture 2 plane are now conjugated to each other. With every lateral position change cut out at the Aperture 2, the optical relay causes also no lateral change at the FSM. This is important because the tip-tilt compensation is supposed to only compensate the angle of incident at the FSM plane like the real telescope output would be adjusted to, to match this behavior.

The AO system is designed for compensating the most dominant aberrations tip-tilt, first. The primary element is therefore the FSM, which tries to compensate by tilting its mirror surface accordingly. The relay lenses before match the conjugate plane and guarantee that only the angle of incident is changed at the FSM. To get the information about the tip-tilt aberrations, a beam splitter is positioned after FSM, redirecting a portion of the beam onto the QPD. A combination of lenses is used to create a detectable spot, consisting of a lens L2 that focuses the light to a spot size and a field lens L3 that increases the measurement field of view. The setup is explained in more detail in Section 3.4.1 and was chosen after testing two other optical designs in Section 3.4.2. The tip-tilt measurement and compensation represents the first subsystem of the AO system.

The second subsystem, which is for compensating higher-order aberrations, is structured similarly. First the DM is positioned in the beam path. Then the beam is directed via another beam splitter to the Shack-Hartmann sensor measuring the wavefront. The lens combination between the FSM and DM serves to conjugate the FSM and DM plane and also resembles an optical relay like the L1 lens combination. The beam diameter remains the same at the surfaces of FSM and DM. The last element, the wavefront sensor has a sensor size of 1.7x1.7 mm therefore, the light beam diameter needs to be reduced. An optical reducer consisting of two lenses (L3, L4) is used, to decrease the beam diameter. Additionally, the wavefront sensor must be conjugated to the DM so that tip-tilt aberrations do not cause lateral beam movement but rather only a change in angle of incident of the light beam. A closer look at the optical design is taken at Section 3.5.

The second beam of the last beam splitter is used for recording the point spread function on a camera. The beam is focused with the lens L7. The camera is placed exactly at the focal point. The resulting spot image on the camera is then used for tuning the

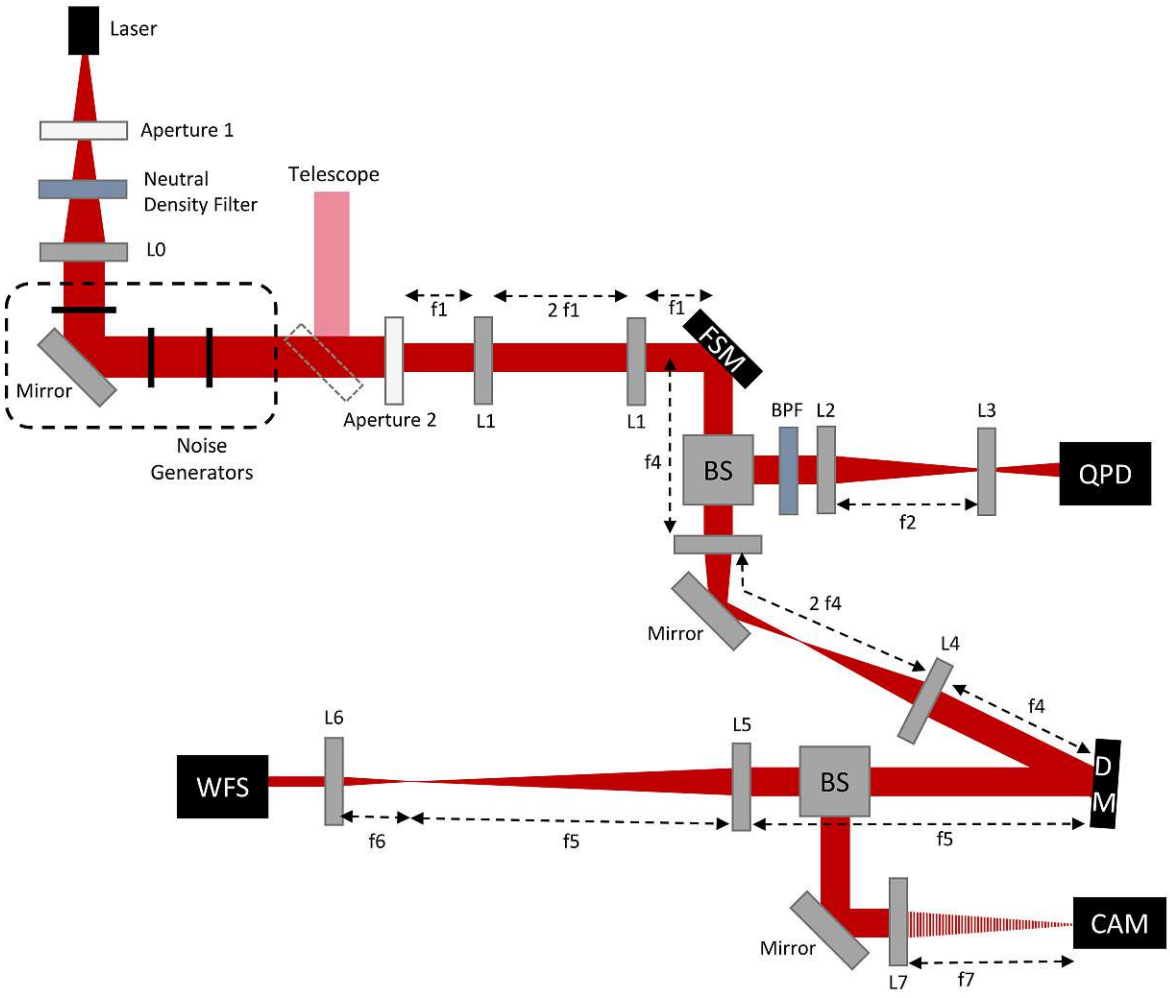

Figure 3.2: Optical setup design, consisting of a laser collimation and intensity adjustment, optical turbulence generator, AO system with conjugate plane matching and a final camera output.

optical system and to evaluate the AO system.

The created AO system represents a compact optical design that is divided into two subsystems. The actual setup was constructed as closely as possible to the optical design and is shown in Figure 3.3. Additional shielding from ambient light is needed and achieved by using aluminum foil and tape. Cardboard covers are also employed during measurements to prevent external disturbances.

3.3 Laser

The reference source is provided by a single mode fiber laser with a wavelength of 635 nm and an output power of 0.5 mW. Due to the single mode fiber it provides a

Table 3.1: List of elements of the optical setup.

Name	Details	Type
L0	f= 250 mm	Thorlabs,LB1056-B-ML, Bi Convex
$L1_1$	f= 50 mm	Thorlabs, LB147-1-B-ML, Bi Convex
$L1_2$	f= 50 mm	Thorlabs, LA1131-A-ML, Plano Convex
L2	f= 200 mm	Thorlabs, AC254-200-A-ML, Achromatic Doublets
L3	f= 50 mm	Thorlabs, LB147-1-B-ML, Bi Convex
$L4_1$	f= 75 mm	Thorlabs, AC254-075-A-ML, Achromatic Doublets
$L4_2$	f= 75 mm	Thorlabs, LA1608-A, Plano Convex
L5	f= 200 mm	Thorlabs, AC254-200-A-ML, Achromatic Doublets
L6	f= 35 mm	Thorlabs, La1027-A-ML, Plano Convex
L7	f= 500 mm	Thorlabs, AC254-500-A-ML, Achromatic Doublets
Aperture 1	13 mm	
Aperture 2	10 mm	Aluminum Plate
BS	50:50 Beamsplitter	Thorlabs, CM1-BS013
BPF	Band Pass Filter	Thorlabs, FLH05635-10
FSM	Fast Steering Mirror	Micro-Epsilon FSM3000
QPD	Quad Photo Diode	Custom made, based on Hamamatsu S5980
DM	Deformable mirror	Alpao, DM69 (69 actuators)
WFS	Wavefront sensor	Imagine Optics HASO3 Fast (14x14 lenslet)
CAM	Camera	ELP 4K USB Camera

spatially well filtered, high quality beam as reference for calibration and evaluation of the AO system. The light intensity can be changed with an adjustable neutral density filter.

3.4 QPD-FSM AO Subsystem

The optical subsystem for measuring and compensating tip-tilt disturbances consists of a FSM and QPD. The optical configuration that connects these two components is crucial for the measurement range and accuracy of the system. The QPD sensor has a sensor size of 5.2x5.2 mm, which limits the maximum laser beam displacement in both axes. The FSM can achieve tip-tilt angles of up to ± 1.5 degrees. By placing the FSM in an angle of 45 degree, tip-tilt changes in the horizontal axis lead to a decreased beam deflection. In the case of 45 degrees the deflection is reduced to a factor of $\frac{1}{\sqrt{2}}$. The diameter of the laser beam can be adjusted and influences the sensitivity of the operating curve of the QPD (Section 2.3.1). The distance between FSM and QPD plays an important role as it acts as an optical lever. Greater distances cause a larger lever and therefore, lead to larger displacements on the QPD's surface.

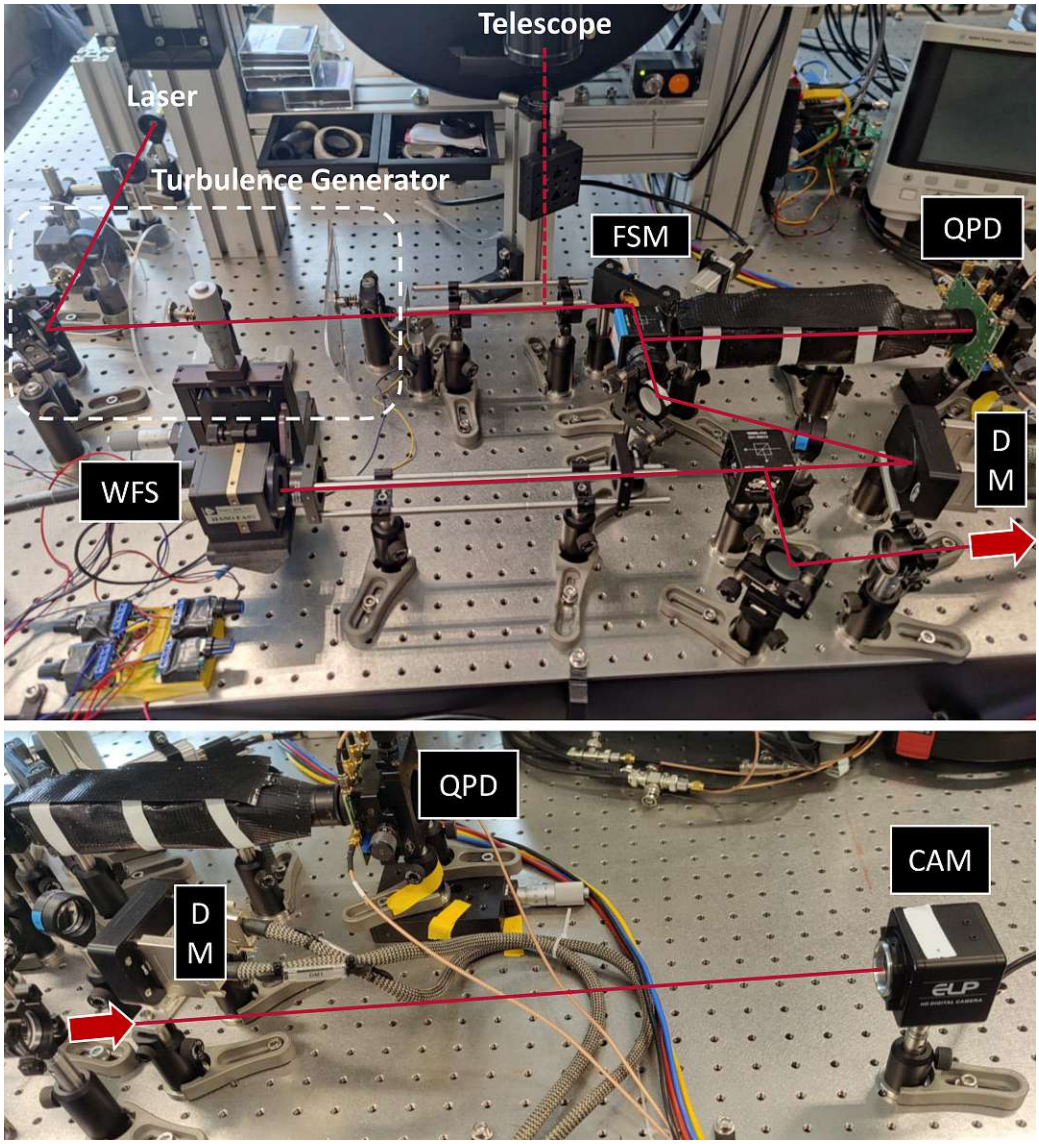

Figure 3.3: (up) Implemented optical setup on a test bench in the laboratory with optional telescope input. (down) Implemented camera.

3.4.1 QPD-FSM Optical Setup

The setup used for measuring tip-tilt disturbances consists of a focusing lens and a field lens and is shown in Figure 3.4. Additionally, a band pass filter is used to block unwanted ambient light and to only pass the desired light beam at a wavelength of 635 nm. The first lens (L2) focuses the laser beam. At the focal point the displacement of the laser beam is at max. The FSM displacement already exceeds the sensor area of the QPD. Therefore, another lens is placed at the focal plane, which is called field lens. This lens redirects the beam back onto the QPD's sensor area without altering the image. The measurement range increases because the QPD can detect larger displacements of the FSM. Furthermore, the use of two lenses, as opposed to one, expands the adjustable parameters that influence the measurement range and accuracy of the optical system.

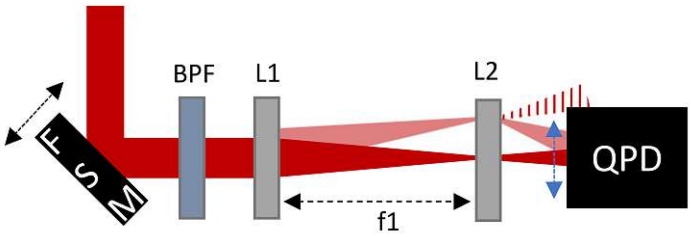

Figure 3.4: Implemented FSM-QPD setup with a bandpass filter, focusing lens and a field lens.

Based on an analysis in Zemax OpticStudio (Figure 3.5), the ratio of the focal lengths between the two lenses (L2/L3) must fall within the range of around 3.2-4.5 to cover the full measurement range of ±1.5 degrees, while maintaining an appropriate detection diameter of the light beam on the QPD. A ratio of 3.2 results in a larger beam diameter on the QPD, while a ratio of 4.5 leads to a smaller one. Larger ratios of around 4, were found to positively impact the measurement accuracy of the QPD. The steeper operating curve of the QPD allows for more accuracy, but sacrifices measurement range. Another advantage of this optical design is that the beam diameter of the light beam stays relatively constant to position changes in lateral direction of the QPD. This is a result of the long focal length of the first lens. Consequently, the main influence in changing the QPD position comes from the deflection of the beam by the field lens. As a result, adjusting the QPD's position allows for an easy change of the measurement range. In the real setup, the QPD was thus placed on a linear stage for easy and quick adjustments.

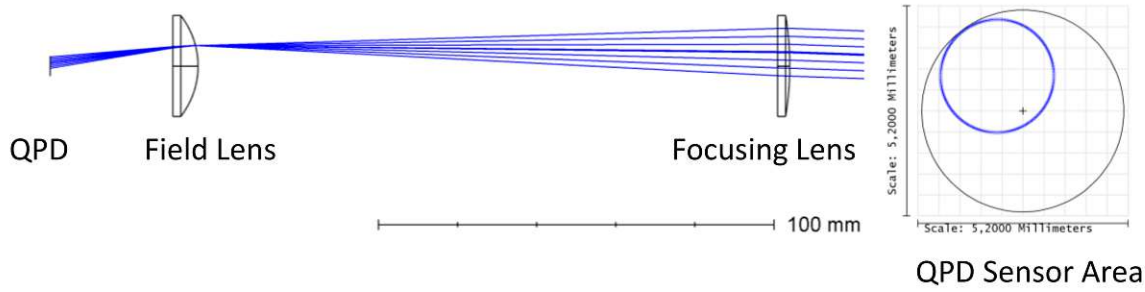

Figure 3.5: Zemax OpticStudio simulation of the implemented FSM-QPD setup, measuring the displacement at the QPD sensor.

In the final optical setup the focal lengths of f_2=200 mm for L2 and f_3=50 mm for L3 were used. This choice results in a ratio of 4, which enables the measurement of the maximum FSM deflection of ±1.5 degrees. To achieve higher accuracies in the implemented control loop the actual measurable deflection was reduced to ±0.2 degrees by changing the QPD position, which results in a higher sensitivity. Therefore, the distance between L2 and the QPD was adjusted until the desired measurement range and accuracy were obtained.

Lessons learned

During the implementation of the optical design in the real setup, several issues arose that were not apparent in the simulation. One major problem is that the QPD not only absorbs the incoming light but also reflects it. As a result, the light reflected by the QPD surface would be again reflected by other optical elements causing an additional point to appear on the QPD surface (Figure 3.6). This reflected point moves in the opposite direction of the actual measurement point and changes the measurement result of the QPD drastically. To address this issue, every optical component is placed at a small angle relative to the optical axis. This ensures that the reflected point is no longer appearing on the detection surface of the QPD, leading to correct measurement signals. Furthermore, the band pass filter, which creates strong reflections, was repositioned. Instead of being directly mounted in front of the QPD sensor, the filter was placed in front of lens L1. Consequently, the distance between the band pass filter and QPD needs to be shielded with tape and aluminum foil to ensure that only the light of the laser beam reaches the QPD sensor.

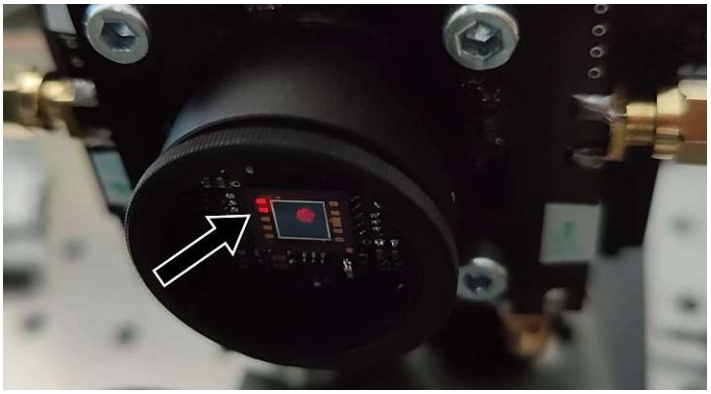

Figure 3.6: Additional point on QPD caused by reflection.

Another advantage of placing the band pass filter in front of L2 is that the incident angle of the laser beam onto the filter is minimized. This is important because large incident angles are found to lead to unexpected behavior changes of the filter. During measurements with large angles, fluctuations in light intensity appear, which negatively impact the measurement signals. This is solved by the different placement.

The precise placement of optical elements, according to the optical design and simulation, is a difficult task. In addition to that, based on the simulation even minor placements errors can have significant impacts on the desired behavior of the optical system. Despite the best efforts to position the optical elements, small errors are inevitably and can alter the expected result. Additionally, the simulations sometimes do not match the real behavior, but they set a good basis to get the desired behavior through small adjustments. On the other hand, a deviation from the optical design is necessary in the placement of the field lens, because if the field lens is placed exactly at the focal point of the lens L2, the noise of the QPD signals increases with unwanted small spikes. This occurrence is happening due to the very small beam size at the focal point and therefore, small contamination or imperfections of the lens lead to additional noise added into the light beam.

3.4.2 Alternative Optical Setups

Besides the implemented optical design, two other designs were tested. The simplest alternative is a single lens system, which focuses the laser beam onto the QPD, thus generating a detectable spot (Figure 3.7 (1)) The distance between QPD and lens is heavily dependend on the lens focal length, as it determines the size of the detectable light spot. Consequently, adjusting the optical lever through a position change of the QPD is limited, because the detectable spot on the QPD needs to have a specific diameter. By using a large focal length the spot size change is smaller by the distance, but the overall distance between lens and QPD is increased. This results in a large optical lever, which in return reduces the detectable measurement range. To counteract the reduced measurement range, a field lens is implemented. In this case, without the field lens, the only option are lenses with short focal length of around 50 mm. The only way to modify the optical lever now, is to put the whole setup closer to the FSM. However, this approach is also limited due to the need of a beam splitter. Therefore, due to few changeable parameters this setup was not chosen. On the other hand, if a simple and straightforward setup is desired, this is a approach.

Another optical design that was tested is the optical reducer (Figure 3.7 (2)). It reduces the beam diameter by a fixed ratio and needs two lenses positioned in a distance equal to the sum of their focal lengths. The large distance leads to a large optical lever, but with the benefit of a fixed beam spot size. The optical lever is however too large to properly measure a wide range of FSM tilt. Additionally, if the QPD is conjugated to the FSM there would be no lateral movement. For these reasons, the optical system was not used after testing.

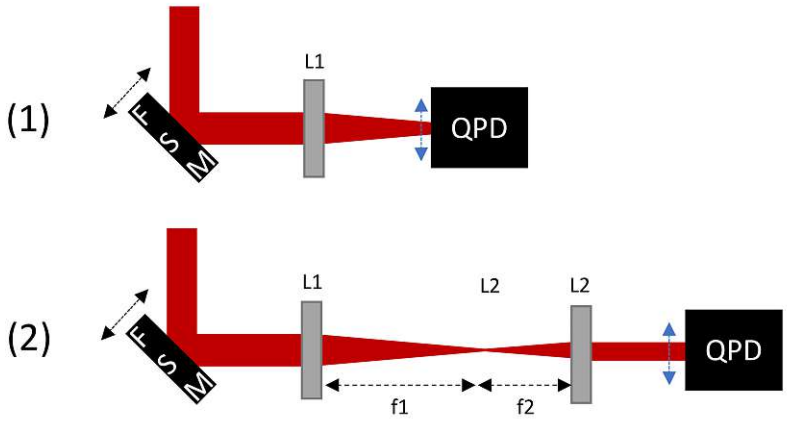

Figure 3.7: (1) FSM QPD setup with a focusing lense; (2) FSM QPD setup with a beam reducer.

3.5 WFS-DM AO Subsystem

The second optical subsystem measures and compensates up to higher order modes. It consists of a Deformable Mirror and a Shack-Hartman WFS. The WFS has a sensor

size of 1.7x1.7 mm, which requires reducing the beam diameter with an optical reducer. This is achieved by using two lenses with a reduction ratio of 0.175. Based on a Zemax analysis L5 was chosen with a focal length of 200 mm and L6 with 35 mm. With these lenses the WFS must be set at a distance of 35 mm, the focal length of the second lens. This ensures its conjugation to the DM and the entrance pupil of the system. Another effect of the optical reducer is that the tip-tilt aberrations get further amplified by the factor of 5.714. For large tilt aberrations, the focal point moves on to the detector area of the next lens of the lenslet or off the detector as whole in case of the point being near the end of the sensor. Therefore, it is crucial to have a good tip-tilt compensation in order to keep the displacements on the WFS within its dynamic tip-tilt range.

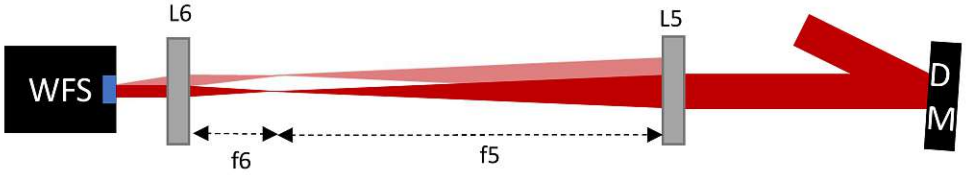

Figure 3.8: Implemented WFS DM setup with a beam reducer.

CHAPTER 4

Controller Design and Implementation

As presented in the previous chapter, the AO system is divided into two main subsystems. In this chapter a control system for each subsystem is designed and implemented, enabling position control of the FSM and DM. First the control loop of the FSM is closed (FSM control). Initially, this is done with the internal sensors. This control loop is used for alignment, setting fixed mirror positions and for calibration. Next the QPD sensor is used and a closer look at the QPD sensor circuit is taken to ensure optimal performance. The control loop itself is implemented in a rapid prototyping system (dSPACE Microlabbox, Paderborn, Germany). After that, the control loop of the second subsystem consisting of WFS and DM is designed (DM control). This control loop is implemented on a PC using Matlab 2015. Each section of the feedback control system is divided into three steps: System identification, where a model of the system is developed; Controller design, where a suitable controller is created; and Controller evaluation, where the implemented control loop is analyzed and evaluated. At last a connection between the two subsystem is established to evaluate the capability of a combined control system design (FSM-DM control) and to implement a static tip-tilt aberration compensation.

4.1 FSM Control loop

The internal sensors of the FSM and the QPD sensor are used to generate a positional feedback control. The resulting feedback control for each axis and sensor is shown in Figure 4.1. Tip-tilt axis can be independently controlled due to a measured difference in cross coupling of over 20 dB. The FSM is driven by a voltage-controlled current source with an integrated current control. The mirror position is measured by the internal sensors or the QPD sensor in Volt. The sensor data is then read by the dSpace and

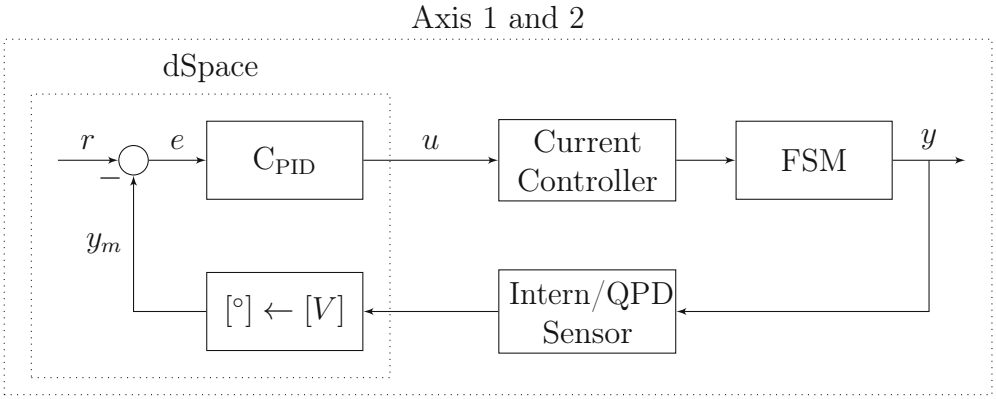

Figure 4.1: Control loop of tip-tilt compensation.

converted into an angular measurement in the transformation is running in real-time on the dSpace and Simulink is only used to program/read out measurement data. In case of the internal sensors, this is done by using a linearization polynomial provided by the manufacturer. In case of the QPD, this is achieved by a constant factor that is calculated by doing a linear fit between internal sensor and QPD sensor signals. The controller is implemented on the dSpace system providing the reference signal for the current controller. The dSpace system operates at a sampling frequency of 50 kHz resulting in a delay of 50 µs, which was also verified by a measurement of output and input of the dSpace system using an oscilloscope. The inner control loop of the current controller operates at a bandwidth of 16 kHz, which is more than 10 times faster than the final outer control loop that is implemented. Therefore, the frequency response of the inner control loop can be assumed to be 1.

4.1.1 QPD Sensor

The QPD sensor is the key component for measuring tip-tilt aberrations in the AO control system. Therefore, it is highly important to optimize the performance of the QPD sensor circuit, in order to achieve best results. The QPD sensor consists of four photodiodes with each having its own amplification circuit that converts the photocurrent into a voltage value and amplifies it. The four signals are then forwarded to the dSpace system for further computations of tip, tilt and sum signal of the QPD. Originally, the tip-tilt and sum signal were directly calculated by analog circuits, but this was changed to allow direct dark current subtraction of the photodiodes currents. The photodiodes themselves operate in photoconductive mode to ensure high speed and excellent precision. The amplification circuit is divided into three stages to ensure high amplification with low extra noise added. Additionally, each amplification stage also acts as a first order low pass filter, refining the signal. First the photodiode current is amplified and converted into a voltage using a transimpedance amplifier. This first stage handles the majority of the amplification and limits the signal to the desired measurement bandwidth of 10 kHz. The amplification is achieved by using 3.3 MΩ resistor, providing a gain of 3.3×10^6. The low-pass behavior is adjusted by a capacitor, which results in a bandwidth of 10 kHz. The following two amplifier circuits

are differential amplifiers. The signal is amplified by a factor of 30 in the second stage and by a factor of 3 in the third stage, achieving the overall amplification of 3.96×10^8. The low-pass filter bandwidths are 78 kHz for the second stage and 26.5 kHz for the third stage. While they do not further reduce the bandwidth of the whole circuit, they eliminate undesired high-frequency noise components that could be introduced by the amplifier circuits themselves or other noise sources after the first amplification.

The custom values of the amplifiers were chosen after identifying that the filter bandwidths of previous used circuits were too low and had too much of an impact in the controller design of the FSM control. As a result the dark photocurrent RMS values of the photodiodes could be lowered by a factor of 3 with an increased bandwidth of 10 kHz. This bandwidth is considerably larger now than that of the closed-loop control system implemented later, and consequently the impact in the controller loop is neglectable. The frequency response of the amplification circuit can now be assumed the constant value of 3.96×10^8.

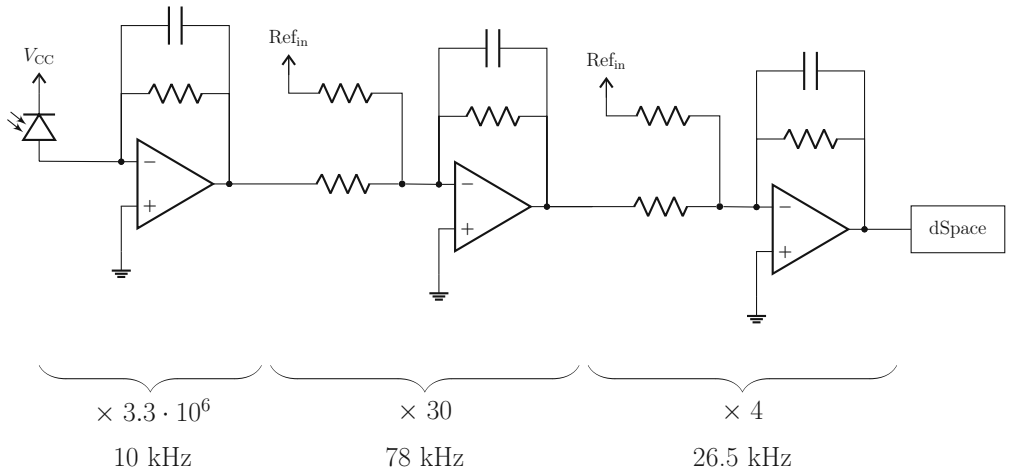

Figure 4.2: Single quadrant amplification circuit of the used QPD circuit.

4.1.2 System Identification

The system identification deals with creating a mathematical model for the FSM system from Figure 4.1 based on measurement data. To achieve this, a linear chirp signal with a trapezoidal window is applied to the system via Simulink and the frequency response is measured. The measurement data contains information about the system behavior consisting of current control, FSM and Internal/QPD sensors and is plotted in Figure 4.4 as a blue line in the bode plots. The lines follow the typical characteristic of a second order system with a mass, spring and damper. The magnitude response starts with the spring line, followed by a resonance peak at the natural frequency and then the mass line with a drop of -20 dB per decade. The phase response shows the expected -180 degree phase drop at the natural frequency for such a system. At a frequency of 2 kHz structural modes appear, which potentially deform the mirror surface. After that the uncertainty of the measurement is highly increased. Following the -180 degree phase drop the phase starts to additionally decrease with higher frequencies. A portion

of that is attributed to the dSpace sampling time of 20 µs. The rest goes with an additional drop in magnitude, which can be modeled with a first-order low-pass filter at 3 kHz. This low-pass filter model is also observable in the given transfer function of the manufacturer and thus indicates a distinct characteristic of the FSM electronics. Another observation is small antiresonance-resonance peaks in magnitude and phase at the mass line of tip-tilt at around 480 and 650 Hz. While they are atypical and do not appear in the manufacture transfer function, they also do not lead to a lasting phase drop or phase drop large enough to cause instability and therefore were ignored in the model fit. The final model fit consists of the second-order system fit, a first-order low pass filter at 3 kHz and a dead time of 50 µs. The mathematical expression for the final model is given by

$$G(s) = K_{Gain} \cdot \underbrace{\frac{\omega_n^2}{s^2 + 2\zeta\omega_n s + \omega_n^2}}_{\text{2nd Order System}} \times \underbrace{\frac{1}{\frac{1}{2\pi \cdot 3000} \cdot s + 1}}_{\text{Lowpass 3kHz}}, \times \underbrace{e^{-2\times10^{-5}\cdot s}}_{\text{Dead Time}} \tag{4.1}$$

where K_{Gain} is the system gain, ω_n the natural frequency and ζ the damping ratio. Figure 4.3 compares the frequency responses of the FSM by QPD and internal sensor measurement. They match each others shape with no large difference in dynamic behavior. This is only after optimizing the QPD circuit. Figure 4.4 shows the transfer functions of the frequency responses and model fits for internal and QPD sensor for each axis. The data lines result in very similar fits. The system behavior of the FSM is thus well identified and modeled, from the perspective of the Simulink system that is also used for the controller implementation.

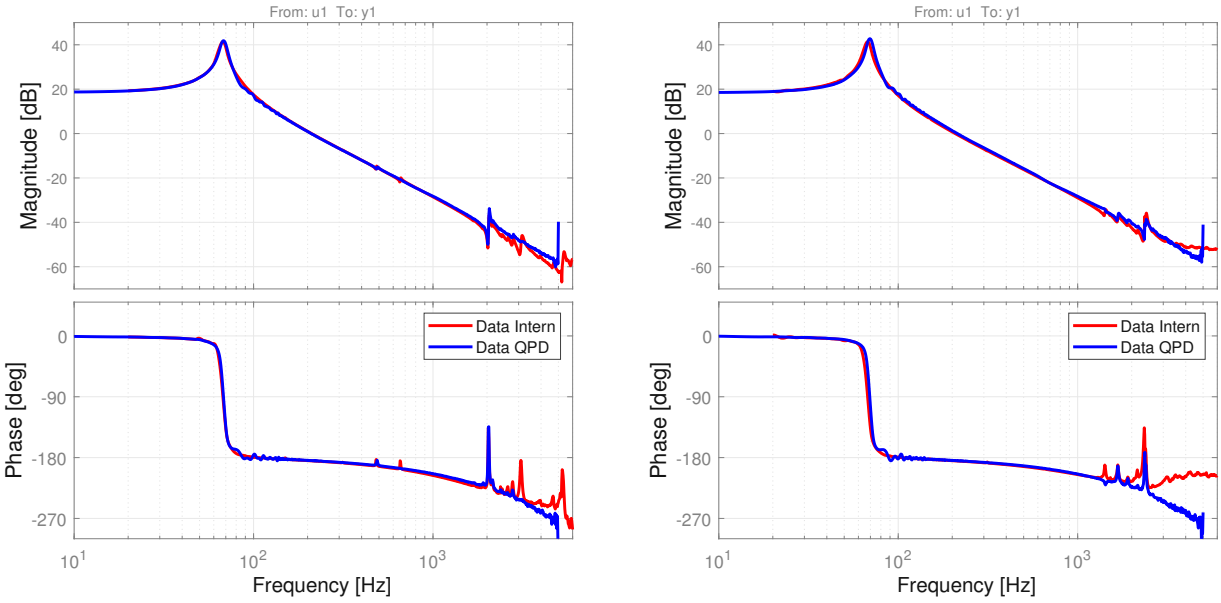

(a) (b)

Figure 4.3: Frequency response data comparison of internal sensors and QPD sensor for (a) tilt and (b) tip.

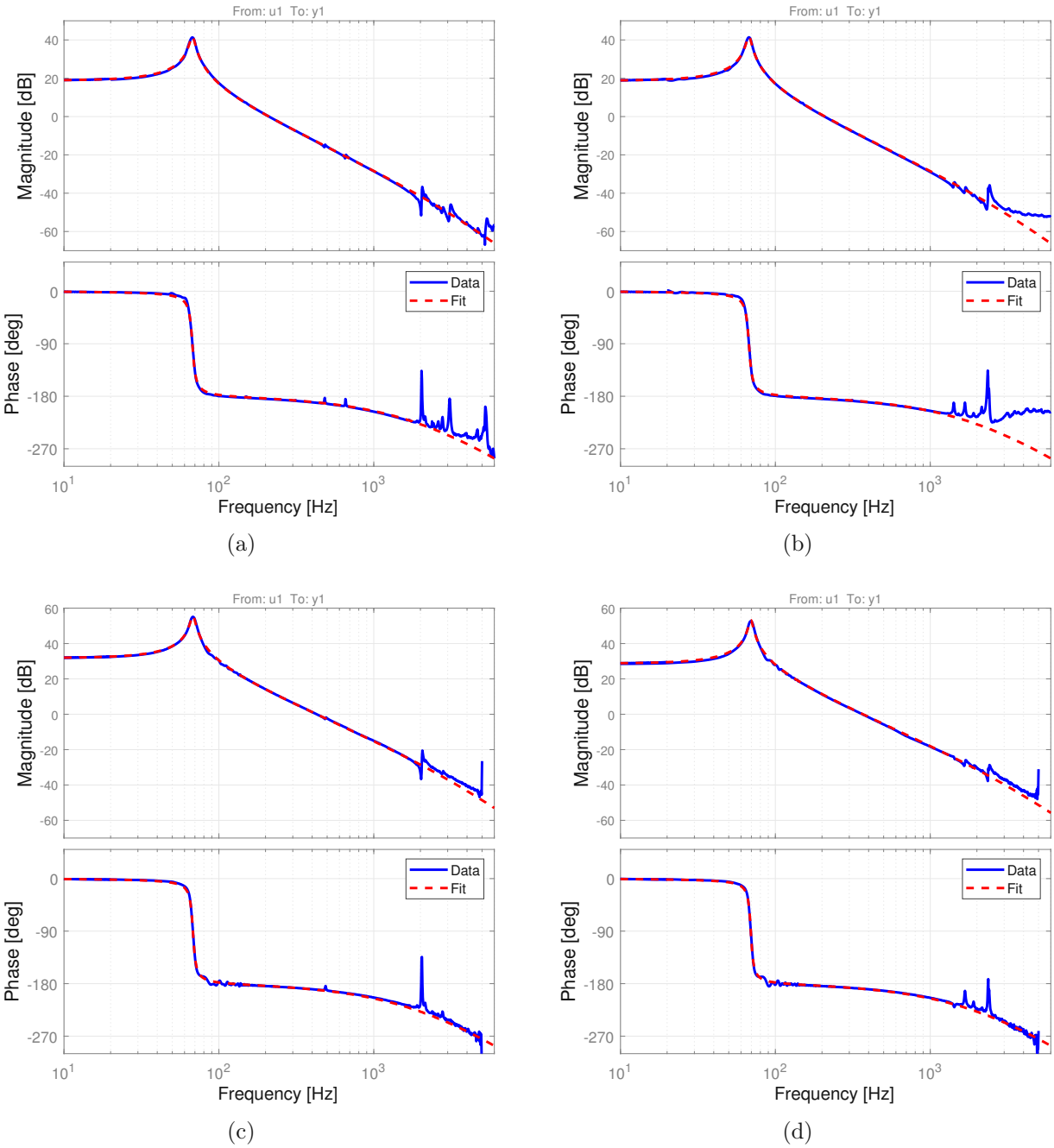

Figure 4.4: Frequency response of internal sensors and fit for (a) tilt and (b) tip; Frequency response of QPD sensor and fit for (c) tilt and (d) tip.

4.1.3 Controller Design

The feedback control loop with the internal/QPD sensor is closed by using a PID controller with a taming term. This allows for a flexible control design with gains that can be adjusted for robustness and performance. The selected tuning method is alpha tuning [55]. The method was developed for low stiffness mechatronic systems such as FSMs, that are showing a double integrator characteristic beyond the suspension mode and are typically controlled along their mass line. In contrast, the controller identification reveals a deviation to the double integrator characteristic, due to a 1$^{\text{st}}$order lowpass behavior at 3 kHz and an additional phase shift caused by the 5 µs time delay. This leads to a difference in phase of $9.5° + 3.6° = 13.1°$ at a frequency of 500 Hz, which increases to a difference of $18.4° + 7.2° = 25.6°$ at a frequency of 1000 Hz. Therefore, with increasing frequencies, the identified system shows a greater deviation from a second-order behavior. Nonetheless, the tuning method was still applied to the second-order submodel system, because the need for maximizing the bandwidth of the feedback control is not the desired goal. As the relevant frequency range for atmospheric disturbances typically is limited to 200 Hz, the relevant frequency range is covered well by the designed controller. If the goal is maximizing the bandwidth, the tuning method needs to be adjusted. With the controller design staying lower than the 1000 Hz, the phase error gets smaller, and the remaining difference can be compensated for with a slightly more robust alpha tuning design that takes this deviation into account.

In general, the alpha tuning method offers an intuitive approach in adjusting the robustness and performance of a control system. The bandwidth of the feedback control can be adjusted by setting the crossover frequency f_c which specifies the frequency at which the 0 dB line of the openloop transfer function is cut, if the system is exactly a second order system. On the other hand the gains at specific frequencies and the phase margin can be adjusted by changing the alpha value. Higher alpha values lead to a larger phase margin, lower gains at low frequencies and higher gains at higher frequencies. Small alpha values lead to the exact opposite. The specific PID Gains K_P, K_I and K_D are then set by

$$
\begin{aligned}
C_{PID}(s) &= K_P + \frac{K_I}{s} + K_D \cdot s, \\
K_P &= \frac{1}{\alpha \cdot G(s)_{s=j\omega_c}}, \\
K_I &= K_P \cdot \frac{\omega_c}{\alpha^2}, \\
K_D &= K_P \cdot \frac{\alpha}{\omega_c} \cdot \frac{1}{,} \underbrace{\frac{s}{\alpha \cdot \omega_c}}_{\text{Taming term}} + 1, \\
w_c &= 2\pi f_c,
\end{aligned}
\tag{4.2}
$$

where α is the tuning parameter and f_c the crossover frequency. Ultimately, for the controller design a crossover frequency of 500 Hz and an alpha value of 3.5 for both

internal and QPD control was selected. This results in a phase margin of approximately 45 °of the open loop transfer function, with the lowpass filter and the time delay included, for all four cases. The exact results are listed in Table 4.1 and the PID and openloop transfer function are shown in Figure 4.5. The plots show the same behavior for both axis and the internal as well as FSM control. With the phase margin of 45 °this outcome holds a promising controller design, which is tested in the next section.

Table 4.1: FSM controller tuning and resulting openloop performances.

	α	$f_{c,\alpha}$	OL PM	$f_{c,0dB}$	OL GM	$f_{c,-180°}$
Intern axis 1	3.5	500	45.6°	517.5 Hz	5.07 dB	1690.4 Hz
Intern axis 2	3.5	500	45.6°	517.5 Hz	5.07 dB	1690.4 Hz
QPD axis 1	3.5	500	45.6°	517.5 Hz	5.06 dB	1690.0 Hz
QPD axis 2	3.5	500	45.6°	517.5 Hz	5.07 dB	1689.8 Hz

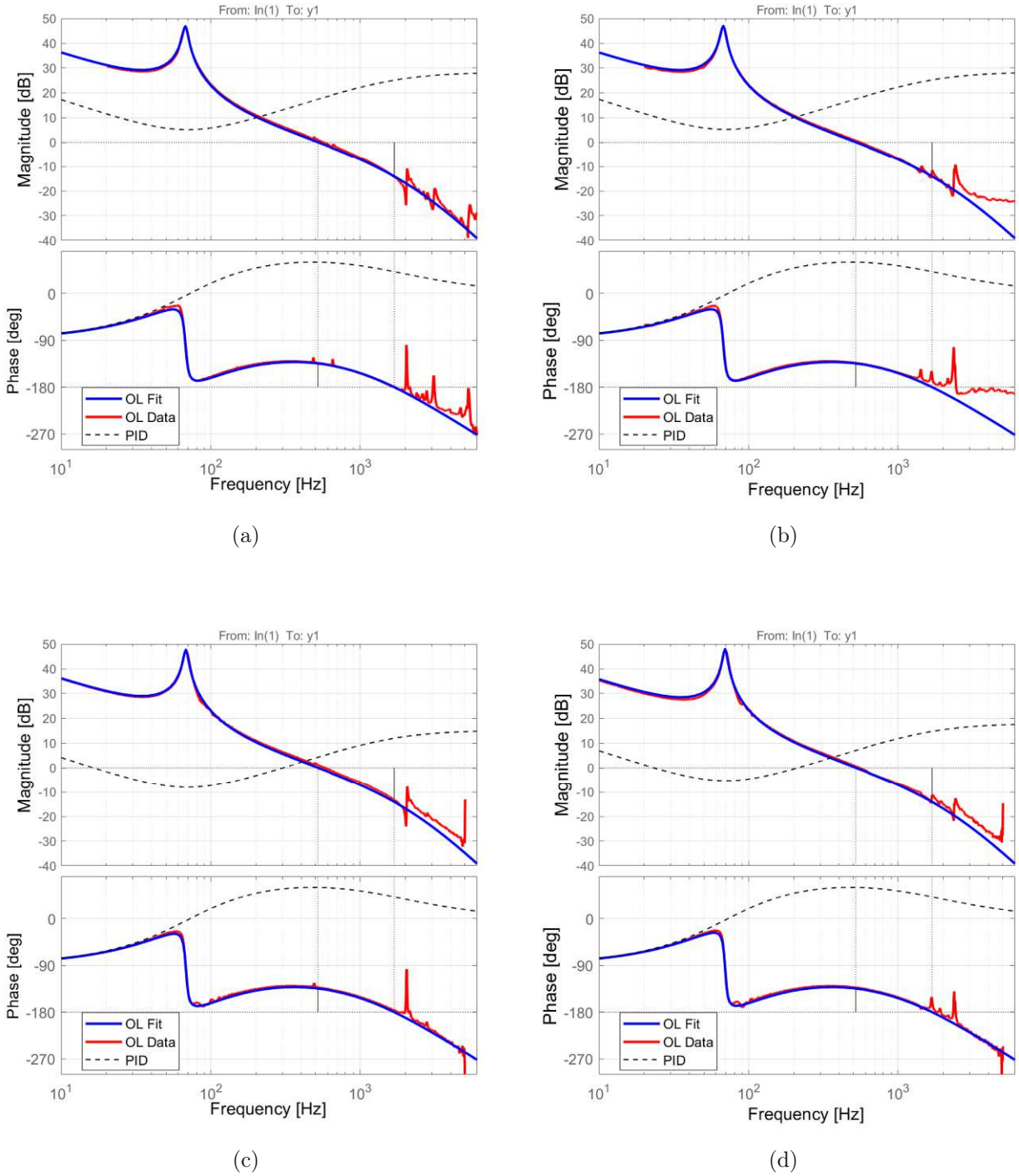

Figure 4.5: Bode plots of measured open loop, fitted open loop and PID controller transfer functions using internal sensors for (a) tilt and (b) tip; Bode plots of measured open loop, fitted open loop and PID controller transfer functions using internal sensors for (c) tilt and (d) tip.

4.1.4 Control Evaluation

For the feedback control evaluation, the controller is discretized with a zero order hold method and the dSpace sampling frequency of 50 kHz. The resulting closed loop system is tested. The system is stable, with an RMS error for a constant position of approximately 2.8 µrad for tip and tilt using the internal sensor control loop. When using the QPD sensor, the RMS values for a constant position increase to 6.0 µrad for tip and 4.0 µrad for tilt. The difference between the two QPD control loop RMS values is attributed to the optical design. The FSM is installed at an angle of about 45°, therefore vertical mirror tilts along the horizontal axis affect the beam only by a factor of $\frac{1}{\sqrt{2}}$. Consequently, the RMS error for tip is greater than for tilt.

The validation of the control loop is done by measuring the sensitivity functions (S) and the complementary sensitivity functions (T). S and T are calculated by

$$\begin{aligned} S(s) &= \frac{1}{1+G(s)C(s)} & S(t) &= \frac{e(t)}{r(t)} & &\text{Sens. Func.} \\ T(s) &= \frac{G(s)C(s)}{1+G(s)C(s)} & T(t) &= \frac{y(t)}{r(t)} & &\text{Compl. Sens. Func.} \\ 1 &= G_{sens}(s) + G_{complsens}(s), \end{aligned} \tag{4.3}$$

where the left side shows S and T for the Laplace domain with G(s) being the system transfer function and C(s) being the controller transfer function. The right side shows S and T for the time domain, with e(t) being the error of the control loop, r(t) the reference input and y(t) the output signal. The signals were measured by the time signals and later calculated in the Laplace domain. The resulting frequency responses of S and T are shown in Figure 4.6. The calculated curves match the measurements and the results are similar between the different sensors and the two axis, with the expected exception of deviations after the structural modes.

The sensitivity function shows disturbance rejection of around -30 dB below frequencies of 80 Hz. The suspension mode of the FSM further improves the disturbance rejection at the natural frequency, which can be seen by the notch. This dip lies perfectly in the frequency range of atmospheric aberrations and thus is positively affecting the compensation of tip-tilt modes. At higher frequencies the sensitivity function rises until eventually surpassing 0 dB and goes into a positive peak. This peak above 0 dB increases disturbances and is called waterbed effect. The waterbed effect occurs when disturbances are suppressed in the low frequency range and as counterbalance disturbances in the higher frequency range are amplified. This is the equivalent of pushing a waterbed. Since atmospheric aberrations are minimal in the frequency range of the positive peak, minimizing or eliminating this effect is not needed. Therefore, it is acceptable for the benefit of greater disturbance rejection at lower frequencies.

For positional control, the complementary sensitivity function is fundamental. It represents the closed loop transfer function and shows how well the input can be followed. It plays a secondary role in the adaptive optics system, because the adaptive

optics system wants to reject disturbances of the optical beam and not to follow a specific trajectory. However, it is important in the internal control loop, enabling the introduction of tip-tilt disturbances for experiments or measurements. Table 4.2 summarizes the calculated and measured bandwidths, the RMS values and the maximum values of S and T.

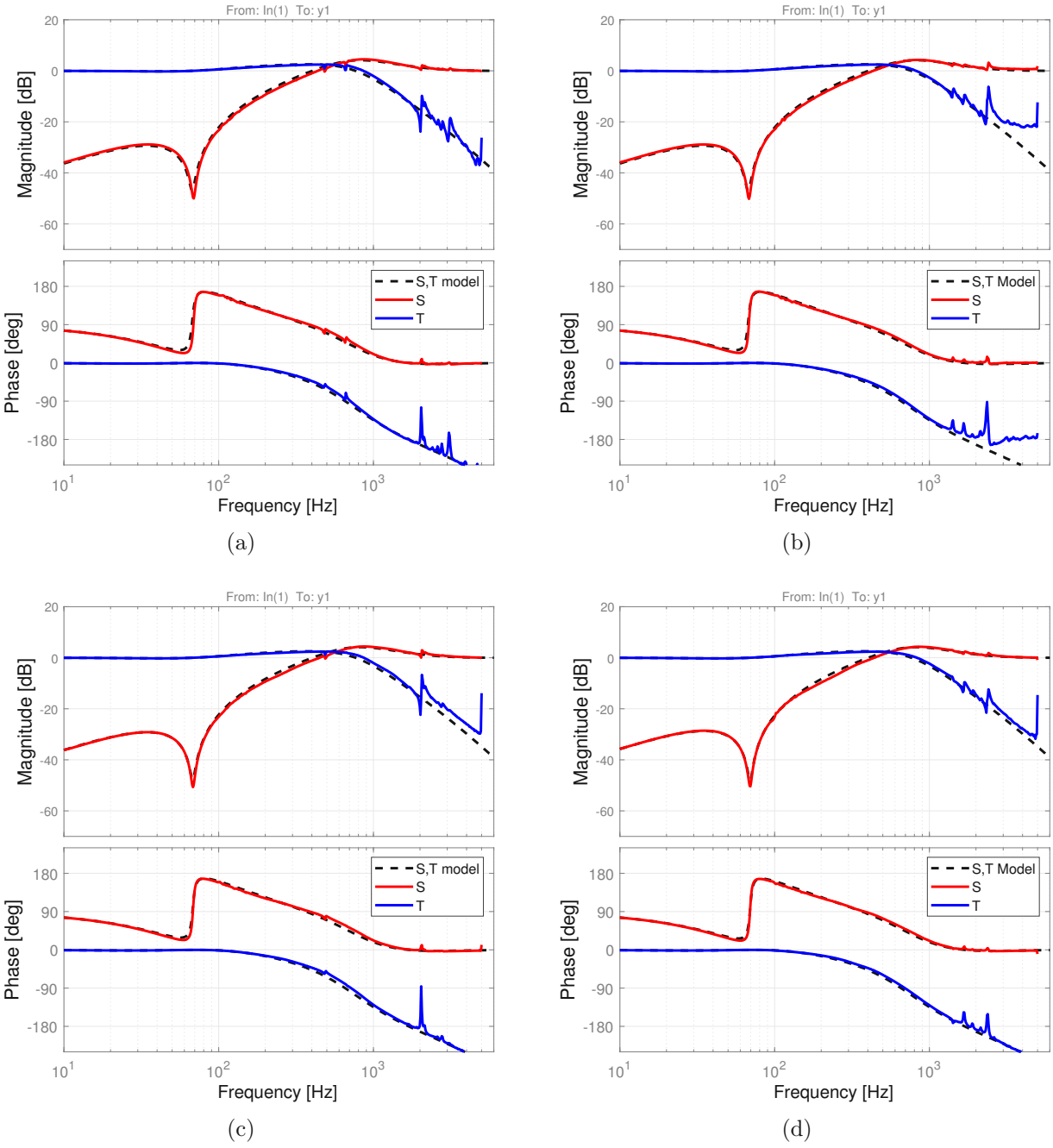

Figure 4.6: Sensitivity (S) and comlplementary sensitivity function (T) measured and caluclated of internal sensors for (a) tilt and (b) tip; Sensitivity (S) and comlplementary sensitivity function (T) measured and caluclated of QPD sensor for (c) tilt and (d) tip.

Table 4.2: Intern and QPD control loop evaluation.

	$\mathbf{S_C(-3dB)}$	$\mathbf{S_M(-3dB)}$	$\mathbf{T_C(-3dB)}$	$\mathbf{T_M(-3dB)}$	**RMS**
Intern ax1	304 Hz	333 Hz	984 Hz	1061 Hz	2 urad
Intern ax2	304 Hz	329 Hz	984 Hz	1021 Hz	2 urad
QPD ax1	304 Hz	335 Hz	984 Hz	1065 Hz	4 urad
QPD ax2	304 Hz	330 Hz	983 Hz	1045 Hz	5.8 urad

	$\mathbf{Max(S_C)}$	$\mathbf{Max(S_M)}$	$\mathbf{Max(T_C)}$	$\mathbf{Max(T_M)}$
Intern ax1	4.1 dB	4.5 dB	2.5 dB	2.5 dB
Intern ax2	4.1 dB	4.3 dB	2.5 dB	2.5 dB
QPD ax1	4.1 dB	4.4 dB	2.5 dB	2.4 dB
QPD ax2	4.1 dB	4.3 dB	2.6 dB	2.4 dB

The results of the FSM control loop show that the sensitivity function reaches -3 dB at 335 and 330 Hz. Consequently, the QPD/FSM disturbance rejection bandwidths is large enough to include most of the atmospheric turbulences.

4.2 DM Control

The DM and WFS are combined in a feedback control system to compensate for up to higher-order wavefront modes. Figure 4.7 displays the block diagram of this control loop. The WFS data processing and the controller are implemented in Matlab 2015 using the Alpao Core Engine Toolbox. The WFS transmits images of the focused light dots created by the lenslet array. By utilizing the center of gravity calculation of the toolbox, the distinct spot coordinates of every lens subaperture are calculated. With the given spot coordinates the slopes can be obtained and the wavefront of the light can be computed by using a modal or zonal approach. The open loop control of the DM is commanded through the transmission of a command vector, which specifies the displacement of each actuator. The sampling frequency of the control loop is dependent on the computation time of the control variable u and therefore directly dependent on the complexity of the control design. The calculation from image to command vector is done in a while loop structure in matlab using the given toolbox functions. Only reading the wavefront slopes results in a sampling frequency of 650 Hz, which is equivalent to a time interval of 1.538 ms. This value drops significantly if the modal wavefront calculation is included and therefore the best approach is to implement a control law that relys only on slope data. To get wavefront data in the modal representation the best way is to save the data, do as minimal calculations as possible in the loop and calculate the values later.

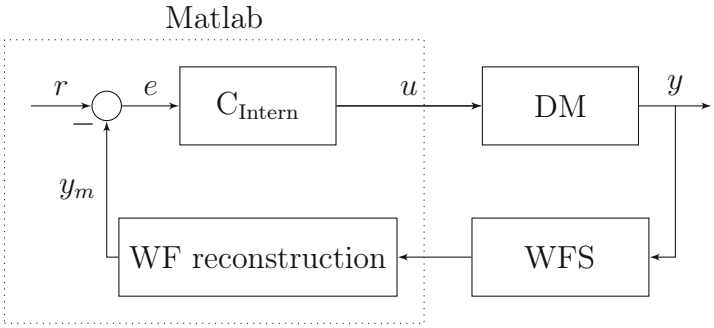

Figure 4.7: Control loop of the higher order compensation.

4.2.1 System Identification

The dynamics and dead time of the system are analyzed to define a mathematical model. In the test report of the DM from Alpao of type DM69 with 69 actuators the system behavior of an actuator is described in a bode plot, which is copied into Figure 4.8. The transfer function shows the typical peak of the suspension mode with the drop in phase at a frequency of 1 kHz. Next the dead time is analyzed by measuring the delay time of moving an actuator with the DM to getting the slope calculation of the WFS. This is done via a square wave signal. The measured dead time was determined to be 4 ms and the corresponding transfer function is also plotted in Figure 4.8. It is evident from the bode plot that the phase drop of the dead time is at significantly smaller frequencies than the phase drop of the actuator dynamics. Additionally, the magnitude is constant

in the frequency range of the WFS. As a result, the overall system can be modeled as a pure time-delay element with a specific gain factor K_Gain. The mathematical model is given by

$$G(s) = K_{Gain} \cdot e^{-4\times10^{-3}\cdot s}, \tag{4.4}$$

where K_{Gain} resembles the system gain.

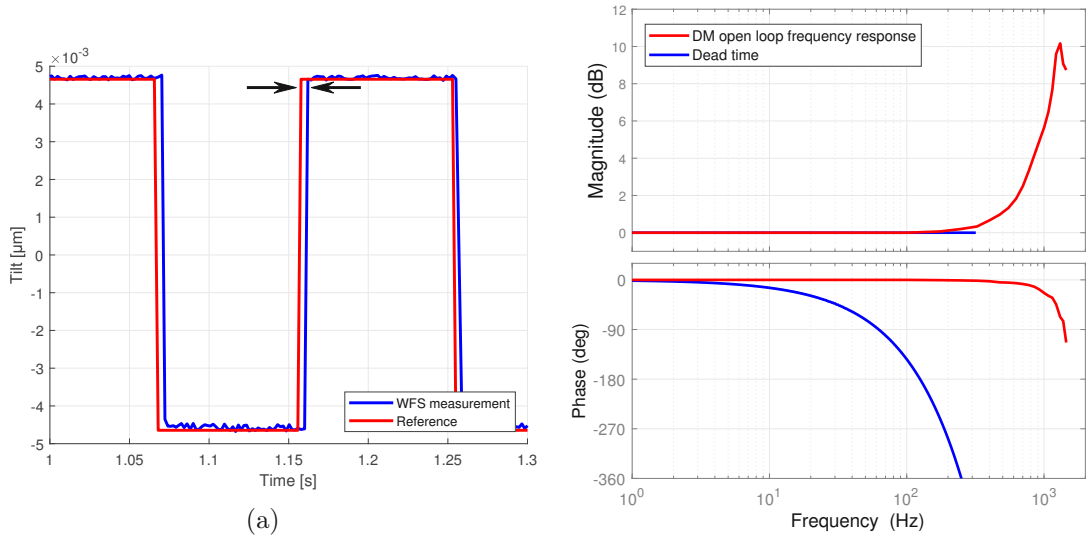

(a) (b)

Figure 4.8: (a) Delay time measurement of actuating a DM actuator with a square wave signal ;(b) Frequency response of measured delay time compared to frequency response of DM given by the manufacturer.

4.2.2 Controller Design

The control law for the DM feedback control is given by

$$Cmd = Cmd_{old} - Gain \cdot [error_x, error_y] \cdot CmdMatrix, \tag{4.5}$$

where Cmd are the cmd vectors, [$error_x$, $error_y$] the slope errors and CmdMatrix the command matrix. The equation represents an integral controller, which is sufficient for system dynamic consisting of only a dead time. In each iteration, the next command vector is calculated by subtracting a value of the previous command vector. The subtracted value is calculated by evaluating the error between the reference slope and measured slope in x and y direction and multiplying that with a gain and the command matrix. The command matrix describes the influence of each actuator on the WFS. This matrix is created by a calibration measurement before the control loop is closed, by measuring the wavefront after moving each actuator individually. The selection of an appropriate gain is done in the next chapter by measurements.

4.2.3 Control Evaluation

The implemented control law is tested with different gains and based on that the mathematical model is tuned. Figure 4.9 (a) shows the different transient responses of the closed loop to a step response based on the calculated first Zernike mode. Lower gains result in improved performance but larger oscillations leading to reduced robustness of the control system. Therefore, a gain of 0.2 is a good compromise between performance and robustness. With the selected gain the gain of the mathematical model can be fine tuned to match the step response. This is shown in Figure 4.9 (b). According to this model the phase margin of the open loop transfer function can be calculated, which is an acceptable 60.2°. With the mathematical model in place, the key parameters of other gains can be easily checked by changing the model accordingly.

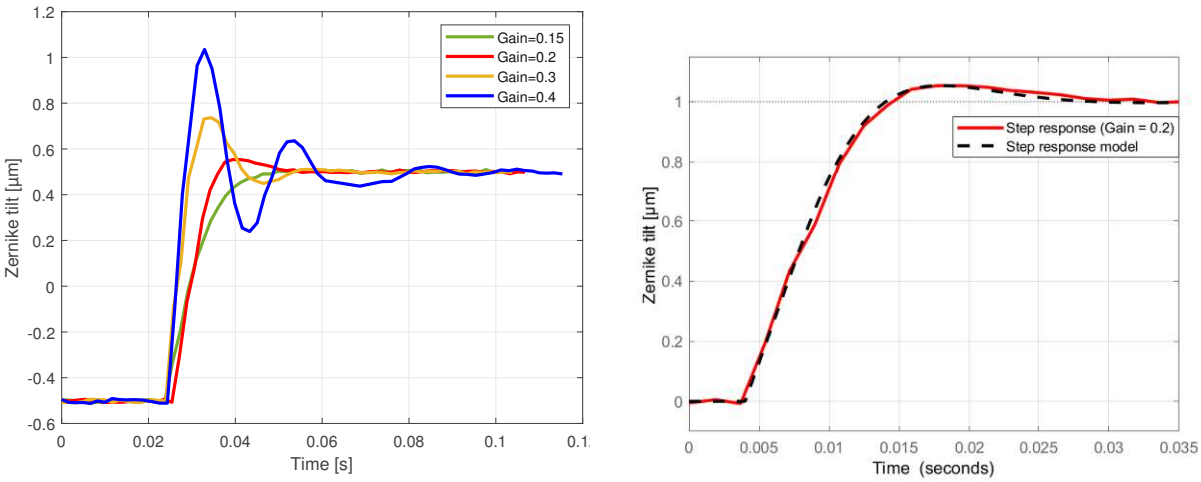

(a) (b)

Figure 4.9: (a) Step responses of closed loop DM control for different gains ;(b) Step response with gain 0.2 and model.

As a validation for the mathematical model and to check certain bandwidths the sensitivity function and complementary sensitivity function are calculated and measured. The measurement consists of multiple measurements of sinusoidal signals at discrete frequencies. The result is shown in Figure 4.10, with the dashed black lines being the calculations and the red and blue lines being the linear connections between the measurement data points of S and T. The S measurement is determined through disturbance rejection by introducing sinusoidal tip-tilts at the FSM. While the DM control loop is closed, the wavefront is measured and the tilt signal is calculated via a modal approach. The counterpart T is measured by applying a sinusoidal signal with different frequencies to the DM and measuring it with the WFS. The measurements match the calculation verifying a good match of the mathematical model.

Table 4.3: Measured characteristics of the sensitivity and complementary sensitivity functions of the WFS/DM loop.

	$S(-3dB)$	$T(-3dB)$	max(S)	max(T)
Model	14.5 Hz	47.4 Hz	4.2 dB	0.0 dB
Measured	13.5 Hz	42.6 Hz	3.9 dB	0.23 dB

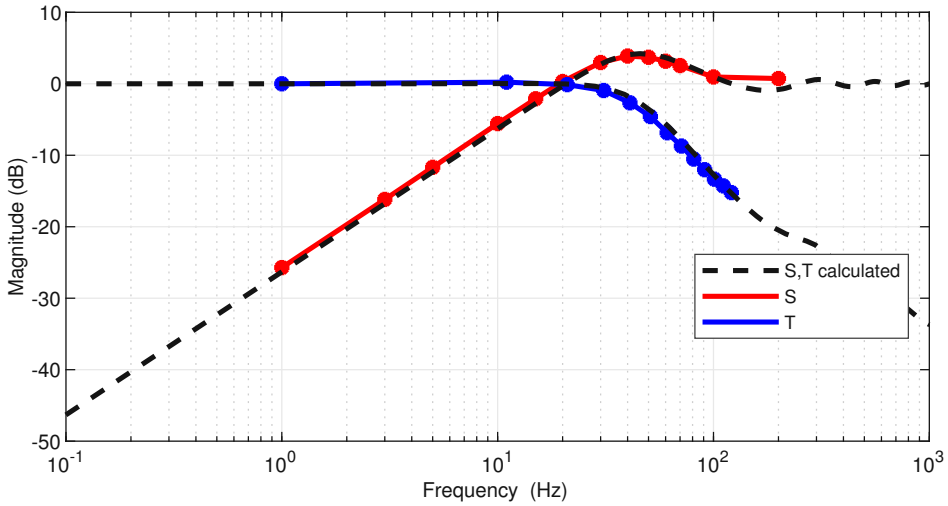

Figure 4.10: Sensitivity (S) and complementary sensitivity function (T) measured and calculated.

The results of the DM control loop show that the sensitivity function reaches -3 dB at 13.5 Hz. Consequently, the WFS/DM disturbance rejection can only compensate for the most dominant low frequency atmospheric turbulences. The waterbed effect at around 40 Hz also leads to some increase.

4.3 Subsystem connection

The control systems of the two subsystems operate independently on different platforms and in series within the optical design. By merging the two systems into one platform, a combined control design could be developed for better performance. However, for now it is not possible to implement the DM control, which is currently run with the Alpao Core Engine Toolbox in Matlab 2015, in the Simulink-dSpace environment with the FSM control. For this reason an alternative concept is tested by connecting the two platforms with a serial communication.

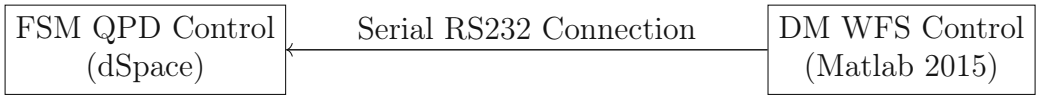

Figure 4.11: Serial connection between FSM control and DM control.

The implemented serial communication allows the exchange of information between the two subsystems (Figure 4.11). The most important information flow is from the WFS to the FSM. It enables the transmission of additional tip-tilt information to the FSM. This is especially needed in the process of aligning the zero tip-tilt points of the two systems. If the points are not identical the result is a constant tip-tilt error at the WFS. Consequently, the DM must compensate for this static tip-tilt error, which has a negative impact on the actuation range and dynamic behavior of the DM. The zero point alignment is achieved by an iterative minimization algorithm that is applied before each measurement.

In addition to compensating the static error, it is also possible to constantly transmit the tip-tilt error of the WFS to the FSM control. However, by constantly sending the tip-tilt information via the serial connection the sampling frequency of the DM control drops significantly from 550 Hz. Consequently, the bandwidth of DM control is also significantly decreased and therefore, dynamic tip-tilt control of the FSM based on WFS measurements is not implemented.

CHAPTER 5

Optical Turbulence Generators

In order to test the adaptive optics system in the laboratory, the output of the telescope needs to be replicated. The new output is created by a collimated laser beam with a diameter of 1 cm. This laser beam is modified to match the atmospheric aberrations, which is achieved by an optical turbulence generator. The perfect imitation of atmospheric turbulences is a challenging task and different approaches can be used, as listed in Chapter 2.6. The main goal of the optical turbulence generator is to replicate the measured noise profile of the satellite "SL16RB" of Chapter 2.5. Two strategies are investigated in this chapter: a DC motor shaker and phase screens out of plexiglas plates. The most accurate replication is characterized and used in the next chapter to test the adaptive optics system on.

5.1 DC Motor Shaker

A straightforward technique for introducing tip-tilt disturbances is to shake a planar mirror in the optical system. For this purpose, a DC motor with an imbalance was fixed on to Mirror 1 (Figure 5.3). The rotating imbalance transmits motion onto the mirror, which then leads to tip-tilt aberrations in the laser beam. While this method is easily integrated, its adjustability is limited. Figure 5.1 shows the measured tip-tilt time signal and spectrum of the shaker and compares it to the SL16RB measurement. The time signal consists of a distinct oscillation and the RMS value is around a third. The spectrum shows discrete peaks, that are slightly above the amplitude of the reference. Both signals do not match the SL16RB measurement and consequently, this method is not suitable to recreate the specific shape of the noise profile. Nevertheless, this method provides a simple solution to introduce disturbances and conduct first tests on the tip-tilt compensation.

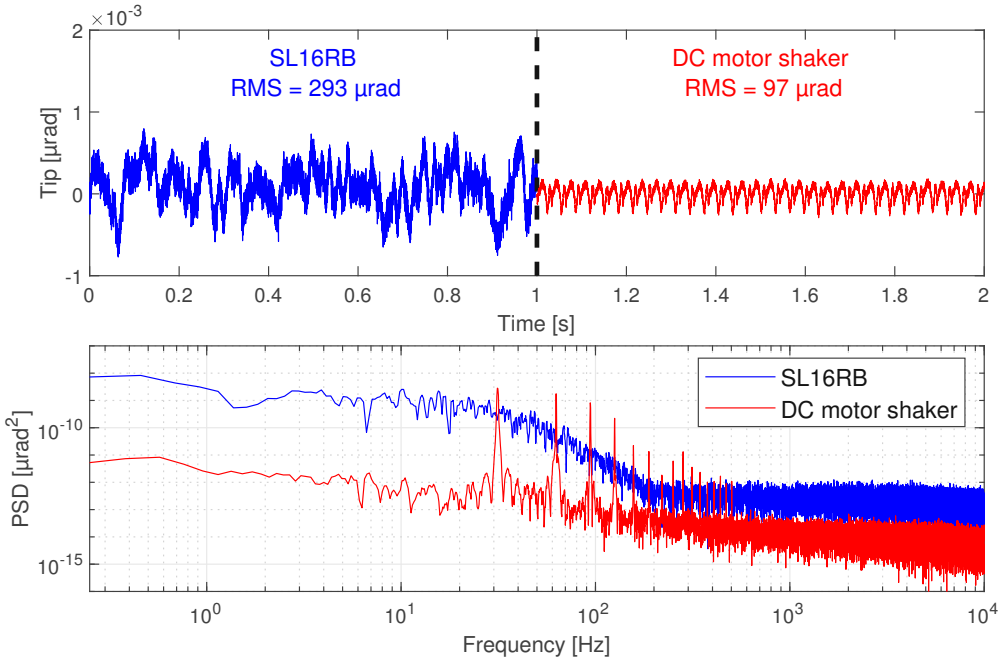

(a)

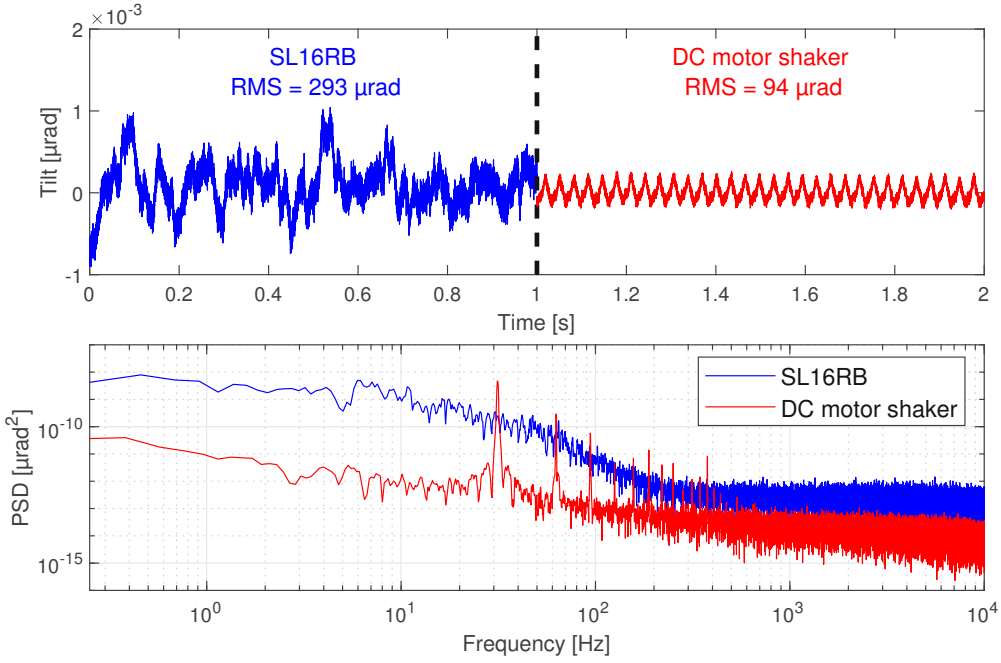

(b)

Figure 5.1: Time signal and power spectral density (PSD, always in $\mu rad^2/Hz$) comparison of SL16RB and DC motor shaker measurement.

5.2 Phase Screens

A more sophisticated approach to introduce atmospheric disturbances is to use rotating phase screens. Phase screens introduce disturbances ranging from tip-tilt up to higher-order modes. A simple way to produce phase screens is to use plexiglass plates that

are either modified through bending or by transparent sprays. Bending a plate can be easily achieved by heating the plexiglas plate with a heat gun. For transparent sprays standard off-the-shelf hairspray can be used.

The process of creating a phase screen is a science on its own. Too much heat from a heat gun produces bubbles or distortions that are too large for a proper WFS measurement. Thin plexiglass plates are more susceptible for errors and therefore only thicker plates are used. Applying too much hairspray leads to too much distortion, which results in interruptions in the WFS measurement. Additionally, if some dirt or dust sticks to the plate while heating or hair spraying the plate, the shadow of such defects makes the plate unusable.

By measuring the QPD tip-tilt signals of a bent and hairspray plate, the time signal and spectrum can be compared with the SL16RB measurement and noise floor. This is shown in Figure 5.2(a) with the left side being the time signals and the right side showing the spectrum. The time signal of the bent plate matches the amplitude of the SL16RB but has a lower frequency. As a result the spectrum of the bent plate matches the magnitude of the SL16RB in lower frequencies but falls of faster at higher frequencies. The typical shape of a Kolmogorov model with the distinct sections of power to -11/3 and -2/3 is not matched. The time signal of the hairspray plate has a much smaller amplitude than the SL16RB, but the shape of the spectrum is very similar to the spectrum of the SL16RB measurement. This confirms the results by previous papers of hairspray being a good imitation of atmospheric turbulences in terms of the spectrum. However, due to the low amplitude of the signal the hairspray plate alone can not be used for the recreation of the SL16RB measurement.

The bent and hairspray plate can also be evaluated with the WFS. The WFS gives insight in the Zernike coefficient values along the different modes, which is a specific distribution for the Kolmogorov model depending on the seeing conditions and the telescope aperture. Figure 5.2(b) shows the sum of the standard deviation in dependence of Zernike coefficients for the bent plate, hair spray plate and noise floor. The x-axis represents the modes removed starting from 0 up to 15, and the y-values are the sum of the standard deviations of the Zernike coefficients. The y-values can be set into relation of the Kolmogorov model following Equation 2.6 but with the error removed greater than 15. Two fitted Kolmogorov distributions are plotted with the D/r_0 ratio adjusted to match the value at 0 modes removed. The fits show that for both plates the drop from 2 to 3 or more modes removed is too small, indicating that the higher order modes make up a too large proportion of the total wavefront error. Other than that the shape is roughly matched.

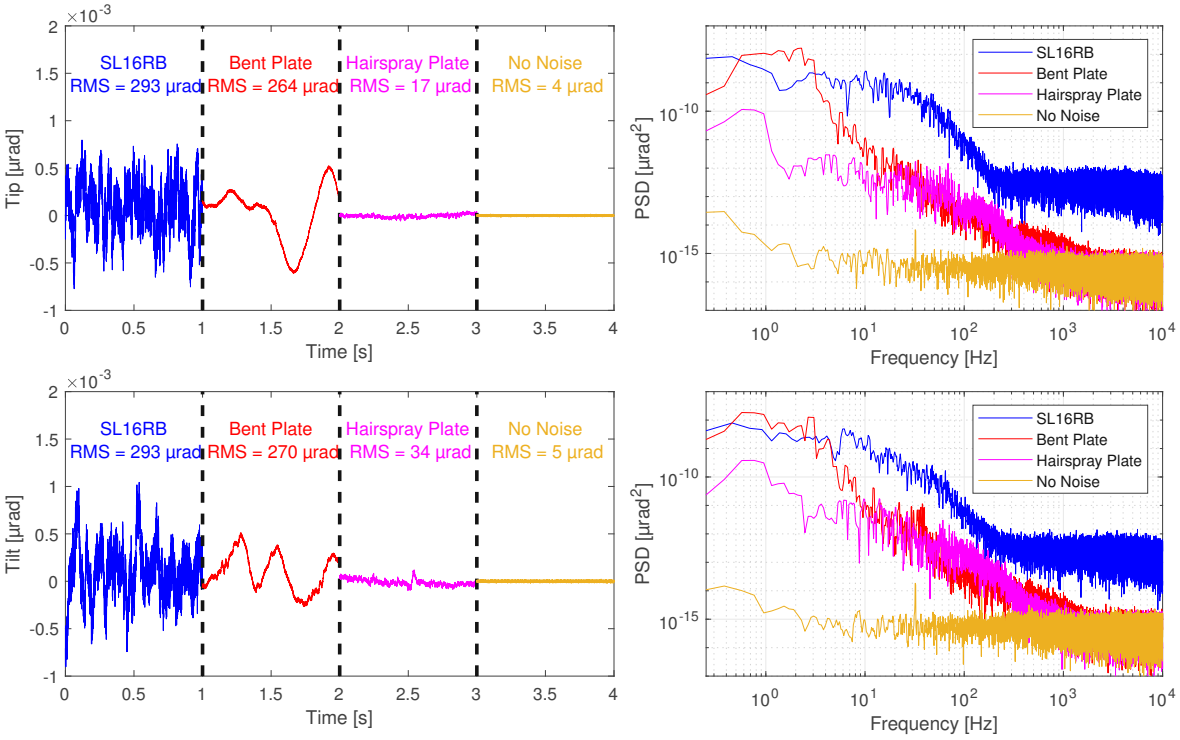

(a)

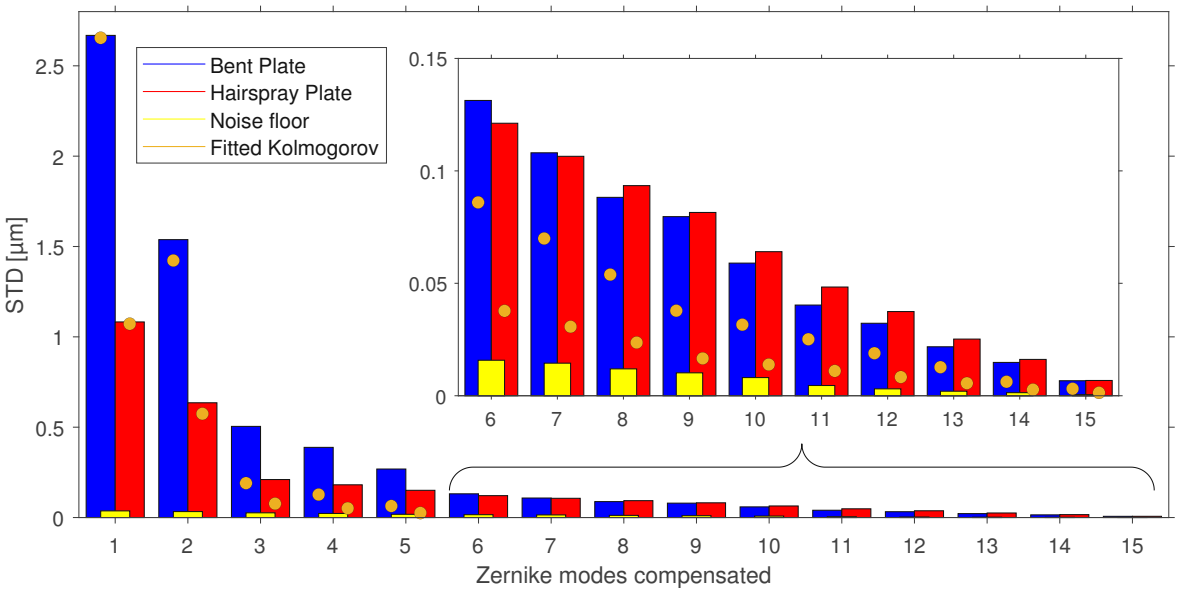

(b)

Figure 5.2: (a) Time signal and spectrum comparison of SL16RB measurement, bent plate, hairspray plate and noise floor; (b) Standard deviation (STD) of Zernike coefficients comparision of bent plate, hairspray plate, noise floor and Kolmogorov fit.

5.3 Tuning of the Optical Turbulence Generator

Based on the knowledge gained on single phase screens from the previous section, an optical turbulence generator consisting of multiple phase screens is built. The goal is to recreate the noise profile of the SL16RB QPD measurement as good as possible and match the distribution of the Kolmogorov model. Different combinations are tested with the best result being a combination of two bent plates and a hairspray plate. Each phase plate can be individually adjusted in speed, allowing for a different and complementary rotational speed of the phase plates. Consequently, the repetition rate of the noise generator can be increased or varied, which also allows for a direct shift of the measured noise spectrum along the frequency axis. The best place for a phase screen turbulence generator is at the conjugate plane which is located exactly at the Aperture 2. However, due to the use of 3 phase plates, limited space and trying to match the RMS value of the SL16RB measurement the phase plates are placed at larger distances to the conjugate plane. As a result the disturbances are introduced at three different spatial positions which complicates the compensation process for the adaptive optics system. This drawback is nevertheless accepted for now.

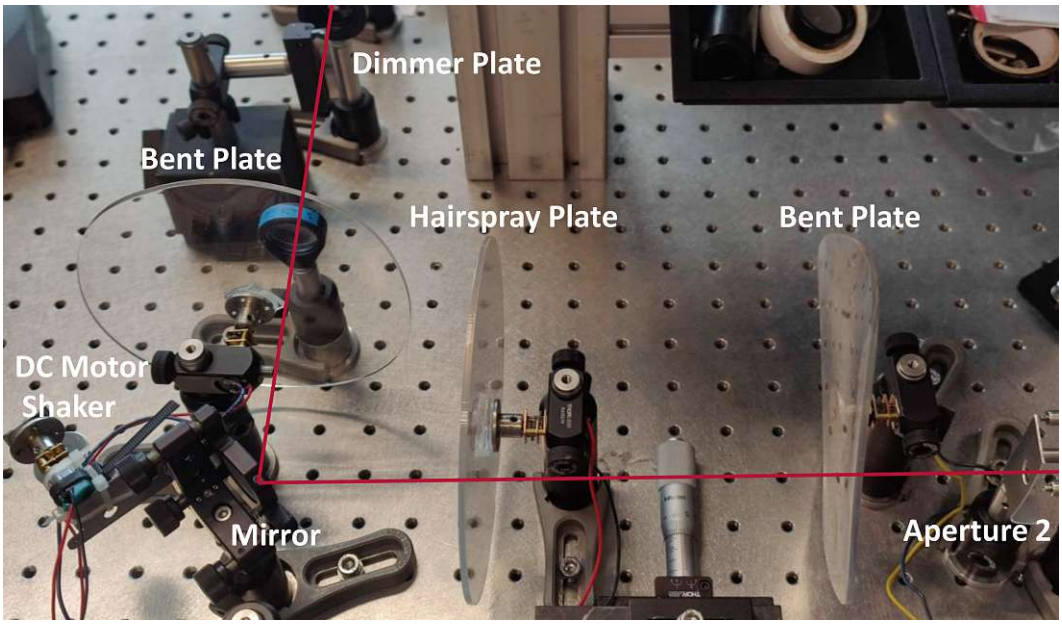

Figure 5.3: Implemented optical turbulence generators. DC motor on plane mirror and 3 phase plates.

The tuned optical turbulence generator is characterized by QPD and WFS measurement in Figure 5.4. The figure shows the tip-tilt signals of the QPD measurement. The RMS value of 293 µrad from the SL16RB is matched with a slightly increased RMS value of 336 and 340 µrad. The amplitude of the time signals are also in the same range as for the SL16RB. The frequency of the time signal of the 3 plate turbulence generator is increased compared to a single bent plate but is still lacking higher frequency components compared to the SL16RB. The measured spectra in the right plots come much closer to the SL16RB measurement than with a bent plate. They still do not match perfectly, but the overall shape is much more similar. All in all best efforts were

taken to match the time signal and spectrum as closely as possible. However, because the reference measurement represents a typical worst-case scenario a 100% match is not necessary.

Figure 5.5 shows the distribution of the wavefront RMS along the Zernike modes in the left plot and the sum of the standard deviation of Zernike coefficients by modes removed in the right plot. The tip-tilt aberrations dominate in the left plot and after that the coefficients make a steep decline, which matches the expected behavior of atmospheric aberrations. The right plot gives a clearer view of how well the distribution of the wavefront error at the Zernike modes removed match the Kolmogorov model. The higher order modes are much more dominant in the 3 plate turbulence generator than in the Kolmogorov model. This indicates that the tip-tilt modes are too low, because the overall curve is matched. All in all, the fit is not perfect, but it allows for a proper and reasonable testing of the adaptive optics system in the next chapter.

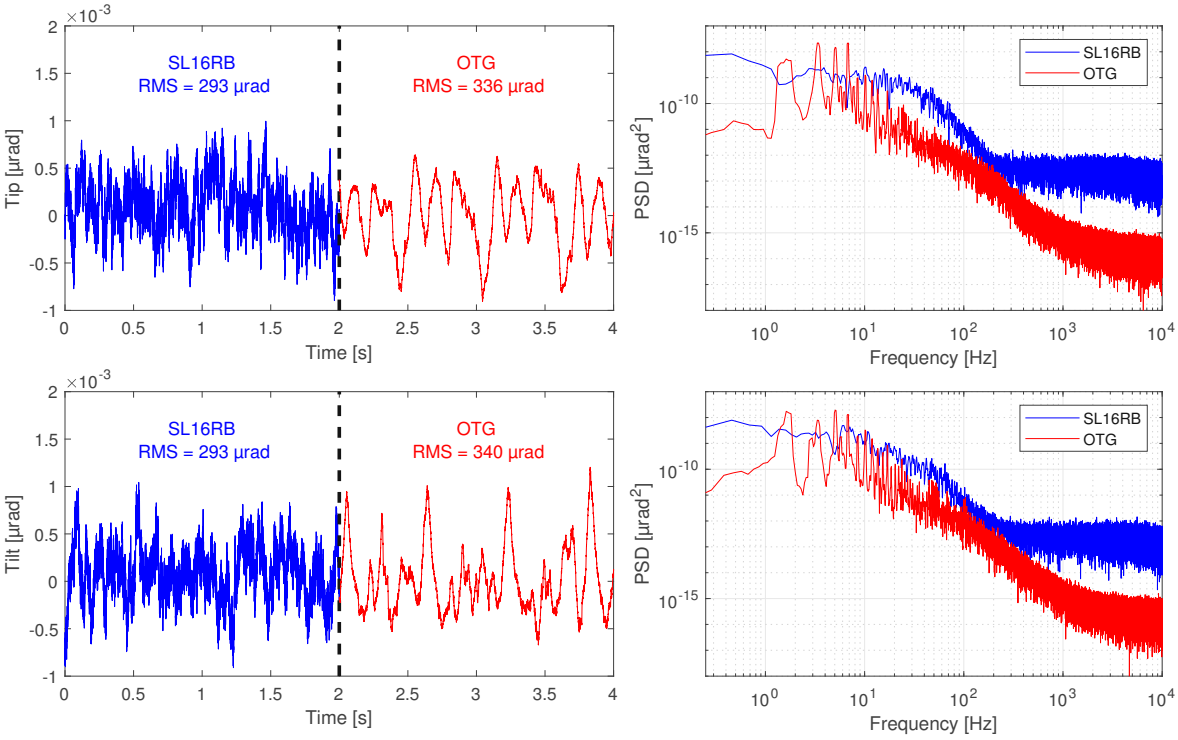

Figure 5.4: Time signal and spectrum comparison of SL16RB and the 3 phase plate optical turbulence generator

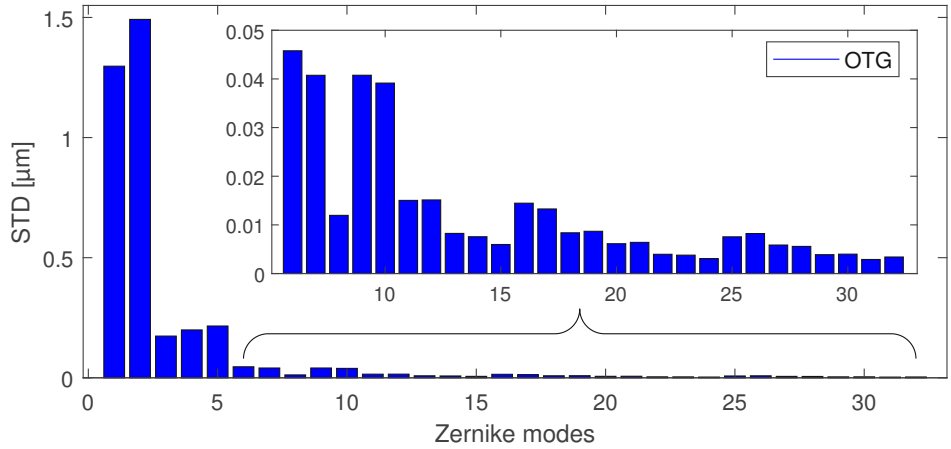

(a)

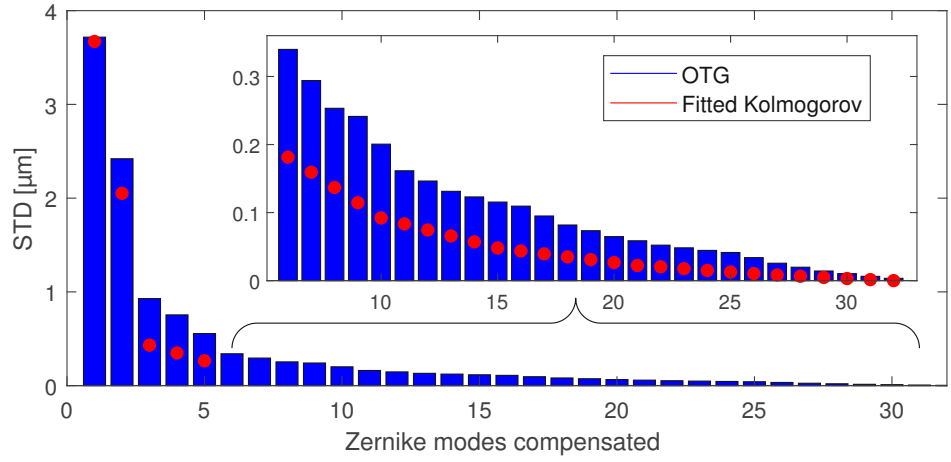

(b)

Figure 5.5: 5.5(a) STD of Zernike coefficients of the 3 phase plate optical turbulence generator; 5.5(b) Sum of STD Zernike coefficients of the 3 phase plate turbulence generator by Zernike modes removed.

CHAPTER 6

AO System Evaluation

In this chapter the AO system is evaluated with the simulated atmospheric disturbance spectrum using the optical turbulence generator from Chapter 5. First the FSM control loop is tested, next the DM control and last both systems combined. Prior to every measurement the static tip-tilt error between FSM and DM control is compensated. The results of the controls are checked with the QPD and WFS by looking at time signals, spectra and distribution of Zernike coefficients. Furthermore, the performance is evaluated by using camera images.

6.1 FSM Control Evaluation

The optical turbulence generator is used to test the tip-tilt compensation. By turning the FSM control on, tip-tilt disturbances are detected by the QPD and compensated with the FSM. As a result the tip-tilt aberrations get eliminated from the beam. The performance and effectiveness of this compensation can be checked with the QPD and WFS.

Figure 6.1(a) and 6.1(b) show the tip-tilt time signal and spectrum of the QPD with FSM control turned off and on. The time signal is reduced from a RMS value of 336 µrad and 340 µrad down to 7 µrad and 9 µrad. Thus reducing the QPD tip-tilt signals by a factor of 48 and 37.8. The performance of one axis is worse due to the FSM being placed at an 45° angle. The spectrum follows a similar trend of reduction. At low frequencies of 0.1 Hz up to the suspension mode the spectrum is reduced by 30 to 40 dB. At higher frequencies the factor is reduced, and the uncompensated spectrum approaches the almost constant level of the compensated spectrum. At around 1 kHz the spectra merge into each other. A distinct drop at around 70 Hz represents the suspension mode of the mirror, which has a positive impact on the disturbance rejection.

In summary, the QPD tip-tilt signals are being reduced to an acceptable low level for frequencies up to 1 kHz and meet the required RMS error of below 10 µrad.

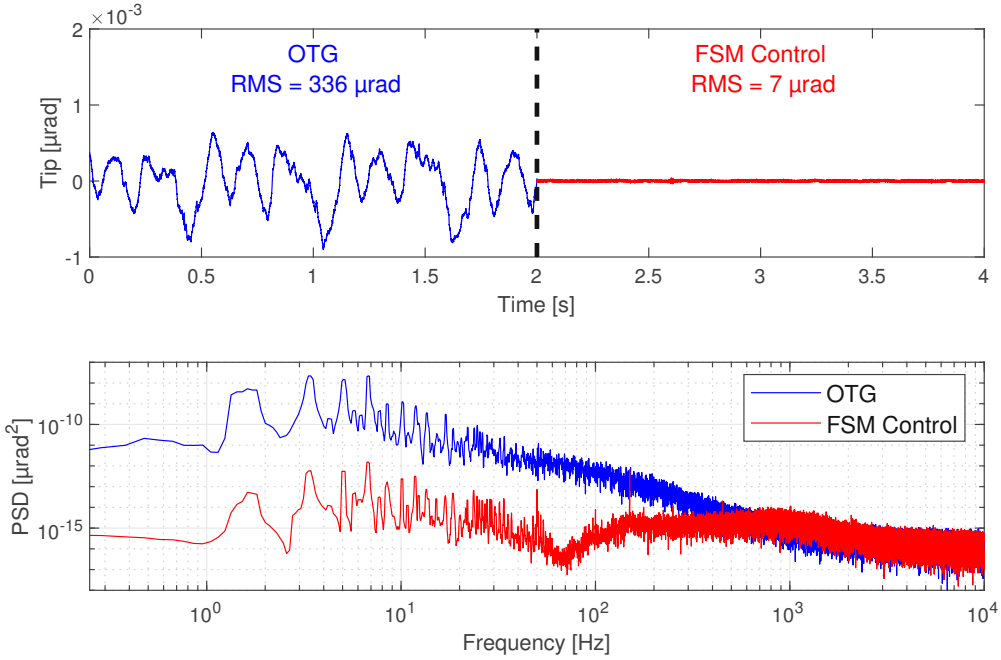

(a)

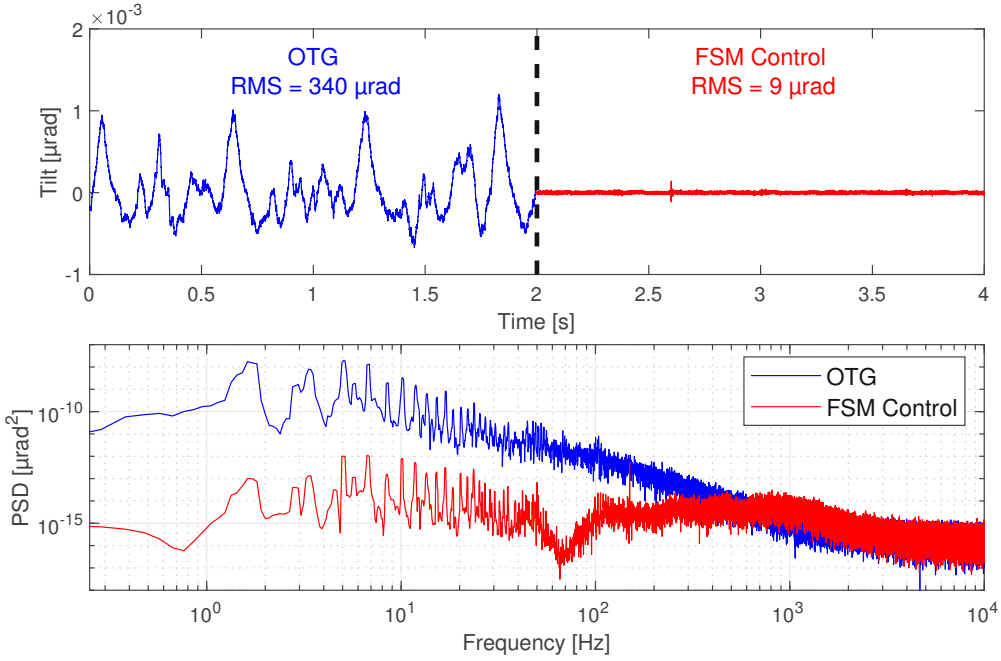

(b)

Figure 6.1: Tip/tilt time signal and spectrum measured by the QPD before and after activation of the FSM control.

The performance of the tip-tilt control is also evaluated with the WFS. In theory, if the FSM control is indeed compensating all tip-tilt aberrations of the optical beam, the WFS should see a similar drop in tip-tilt aberrations. Besides that, the total wavefront RMS error should also drop significantly, because tip-tilt aberrations make up the largest part of the noise distribution. Figure 6.2 summarizes the results of the WFS measurement. The plot on top shows the time signal and spectrum of the RMS wavefront error. The plot in the middle displays the distribution of the wavefront error along the Zernike modes and the table on the bottom summarizes the middle plot by the calculated Zernike coefficient changes. The time signal of the RMS wavefront error drops from a RMS of 2.83 µm to 0.47 µm, which corresponds to a factor of 6.02. A similar trend can be seen in the RMS wavefront error spectrum. With the FSM control turned on, the spectrum drops around 20 dB for low frequencies up to around 10 Hz and stays below the no control spectrum for frequencies up to 300 Hz. All in all, an already clear reduction in the RMS wavefront error is achieved by the FSM control. From the distribution of the RMS wavefront error along the different modes, the impact of the FSM control can be further analyzed. Tip-tilt aberrations drop to 11.4 % and 7.6 %, which is only a factor of 8.77 and 13.58. Compared to the results of the QPD measurement this is much less of a reduction. On the other hand there are also slight reductions in the higher order modes, which should theoretically not be influenced by a tip-tilt compensation. Nevertheless, the AO system profits of a significantly reduced tip-tilt error.

The question arises as to why the WFS does not measure the same reduction of tip-tilt aberrations. The alignment and optical elements play an important role in how well the tip-tilt compensation is received at the WFS. Although a lot of time was used for the alignment process, it is better to additionally use a camera and WFS to check every placement of an optical element in such a large optical system. On top of that, the optical design can be further optimized by reducing the length between FSM and WFS, which reduces the lever for misplaced optical elements. Apart from the alignment, the difference can also be due to the different measurement principles of QPD and WFS. Changes in the spot shape can change the tip-tilt signals of the QPD and lead to a different tip-tilt signals. By comparing the tip-tilt signals of QPD (low pass filtered to bandwidth of WFS) and WFS without any control in Figure 6.3, the two signals can not be perfectly matched. Peaks of the WFS measurement appear to be higher and lower than that of the QPD measurement, which indicates clear differences in the two measurements. Another reason can be non-uniform intensity changes of the beam, which lead to changes in the QPD tip-tilt signals. Further experiments were taken on uniform light changes. By varying the adjustable neutral density filter the light intensity is changed and the tip-tilt with active FSM control is checked at the WFS. With a perfect normalization of the QPD tip-tilt signals by the QPD sum signal, the tip-tilt signals should not change at the WFS. However, intensity changes in the range of the optical turbulence generator lead to observable changes in the tip-tilt signals of the WFS. This adds another reason why the reduction at the WFS is not the same as at the QPD.

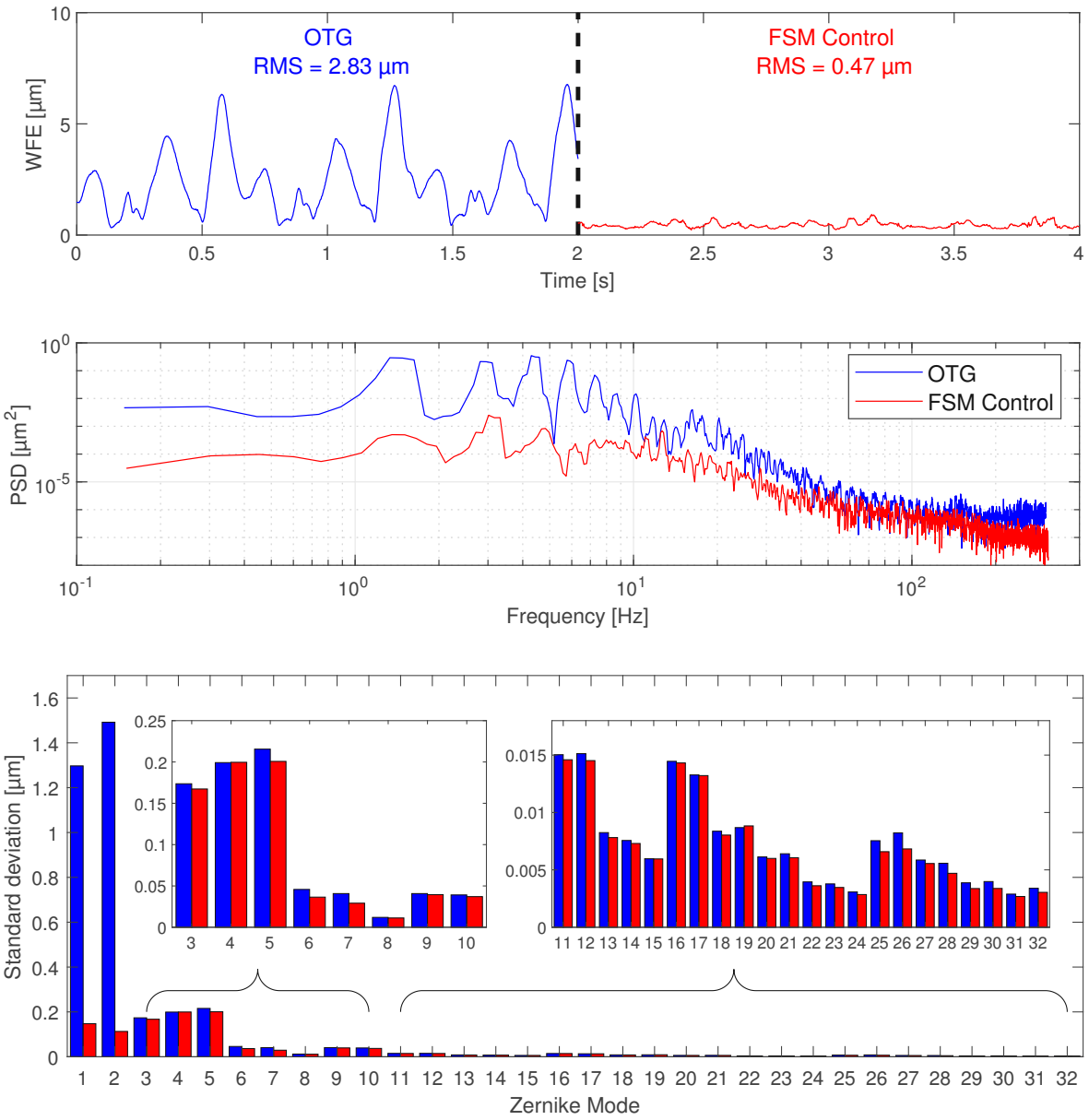

Modes	1-32	1	2	3	4	5	6	7	8-32
Ratio	30.5%	11.4%	7.6%	96.4%	100.2%	93.1%	79.7%	71.5%	95%

Figure 6.2: WFS measurements before and after activation of FSM control. From top to bottom: RMS wavefront error over time, spectra of RMS wavefront error, STD of Zernike coefficients, Value changes of STD of Zernike coefficients.

6.2 DM Control Evaluation

The DM control is tested in normal operation mode by compensating all modes including tip-tilt. Compared to the QPD/FSM control the DM/WFS has a lower bandwidth and a smaller actuation range in the tip-tilt compensation, but can compensate up to higher order modes. Improvements in the wavefront error and in all modes are expected, but

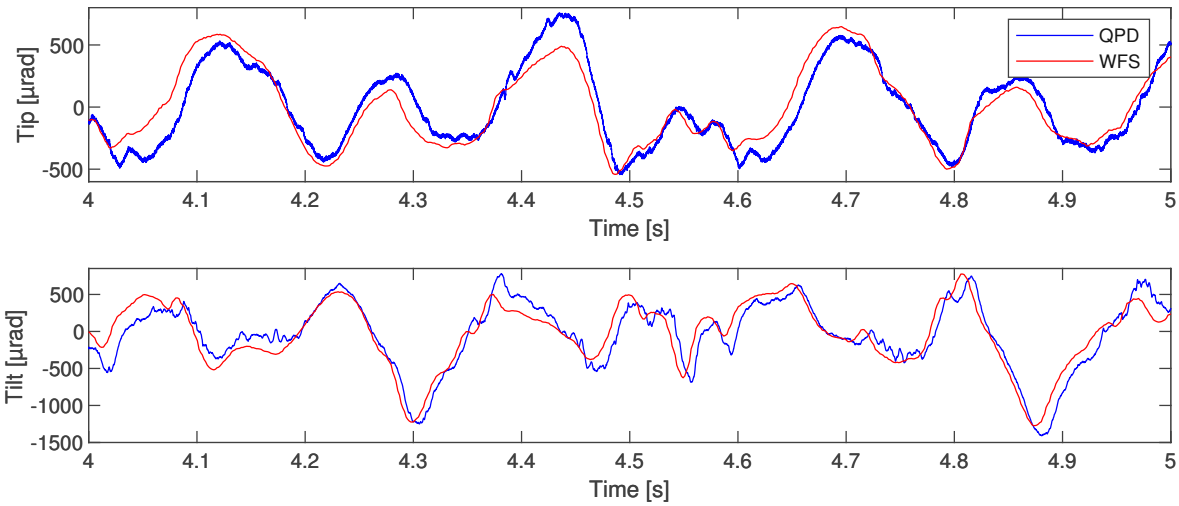

Figure 6.3: Comparison of measured tilt signals by WFS and QPD sensor.

not in the scale of the FSM control due to limited achievable bandwidth of the DM control.

Figure 6.4 shows the WFS wavefront error time signals and spectra in the top plots, the change in STD of Zernike coefficients in the middle plot and the specific values of the change in STD of Zernike coefficients in the bottom table. The time signal of the RMS wavefront error drops from a RMS of 2.83 µm to 0.62 µm, which corresponds to a factor of 4.56. Therefore, the DM control performs worse than the FSM control which has an improvement of 6.02. The resulting spectrum gives insight in why the improvement is reduced. The spectrum of DM control is lowered up until 10 Hz and increased at frequencies of over 30 Hz. The resulting spectrum corresponds to the sensitivity function of DM control loop with a bandwidth of 13.5 Hz and a waterbed effect that increases the aberrations in the relevant range of 20 to 100 Hz. The decrease of the spectrum in the lower frequencies up to around 10 Hz ranges from 10 to 100, which is 10 to 20 dB. The reduced bandwidth of the DM control compared to the FSM control results in worse improvement of the overall wavefront error. The distribution of the RMS wavefront error along the different modes shows where the improvement is taking place. Tip-tilt modes are reduced to 33.5 % and 28.9 %, which is significantly worse than the 11.4 % and 7.6 % of the FSM control. However, the benefit lies in the reduction of higher order modes with a drop of 42.8 % to 77.6 % from mode 3 to 7, which is not achieved by the FSM control. At even higher order modes this trend changes and the STD of the Zernike coefficients starts to increase. The DM control causes a total increase of 130 % in modes 8 to 32. Therefore, the WFS/DM is beneficial for higher order modes ranging from 3 to 7 and 9, which dominate the wavefront error.

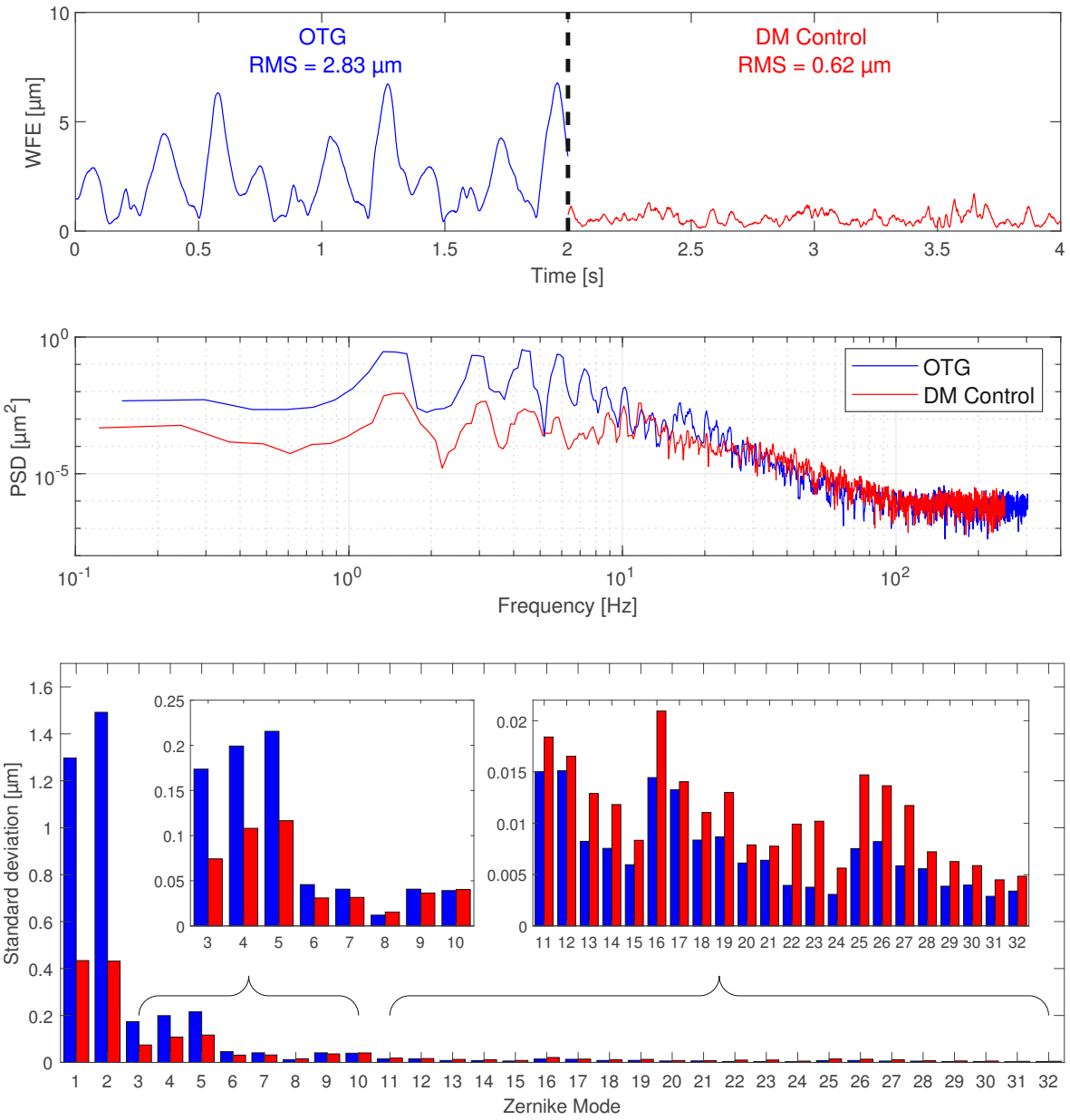

Modes	1-32	1	2	3	4	5	6	7	8-32
Ratio	41.9 %	33.5 %	28.9 %	42.8 %	54.3 %	54.1 %	67.7 %	77.6 %	130%

Figure 6.4: WFS measurements before and after activation of DM control. From top to bottom: RMS wavefront error over time, spectra of RMS wavefront error, STD of Zernike coefficients, Value changes of STD of Zernike coefficients.

6.3 FSM-DM Control Evaluation

FSM control and WFS/DM have been individually tested and characterized. The next step is to test them both combined. To combine the two controls (FSM-DM) it is a valid approach to activate both in series. The FSM control has a sensitivity function bandwidth of 335 and 330 Hz, which is more than 10 times greater than the sensitivity

function bandwidth of the DM control. The QPD sensor is also placed before the DM. Therefore, the two controls in series make the equivalent of a cascaded feedback control with the FSM control being the inner and faster control loop, and the DM control being the slower outer control loop. This implies that the DM control does not register any dynamic behavior of the FSM control, which makes the operation of both system in series valid.

Figure 6.5 shows the results of FSM-DM control activated. The time signal of the total RMS wavefront error is reduced from 2.83 µm to 0.26 µm. This makes a total improvement of a 10.88 factor. The spectrum of FSM-DM controls active is further reduced in the low frequencies up to 10 Hz to reduction of about 25 dB. Both controls have a good suppression in that range. At higher frequencies the spectrum is slightly increased, because of the DM control. As a result the total spectrum appears to flatten out over the frequencies. The distribution of the wavefront error along the Zernike coefficients show a reduction up to mode 10. Tip-tilt aberrations are decreased to 9.4 % and 8.6 %, which compared to the FSM control of 11.4 % and 7.6 % is an improvement in the tip mode and a small reduction in the tilt mode. Combined, this results in a small improvement. Higher order modes from 3 to 7 improve around the same as with the DM control, ranging from 44.5 % and 75.6 %. Higher order modes from 8 to 32 are increased to 107.4 %, which is less than with the DM control. All in all, the total reduction from mode 1 to 32 is 23.8%. This result is 6.7 % better than the FSM control and 18.1 % better than the DM control, making the combination of both with FSM-DM control the best result.

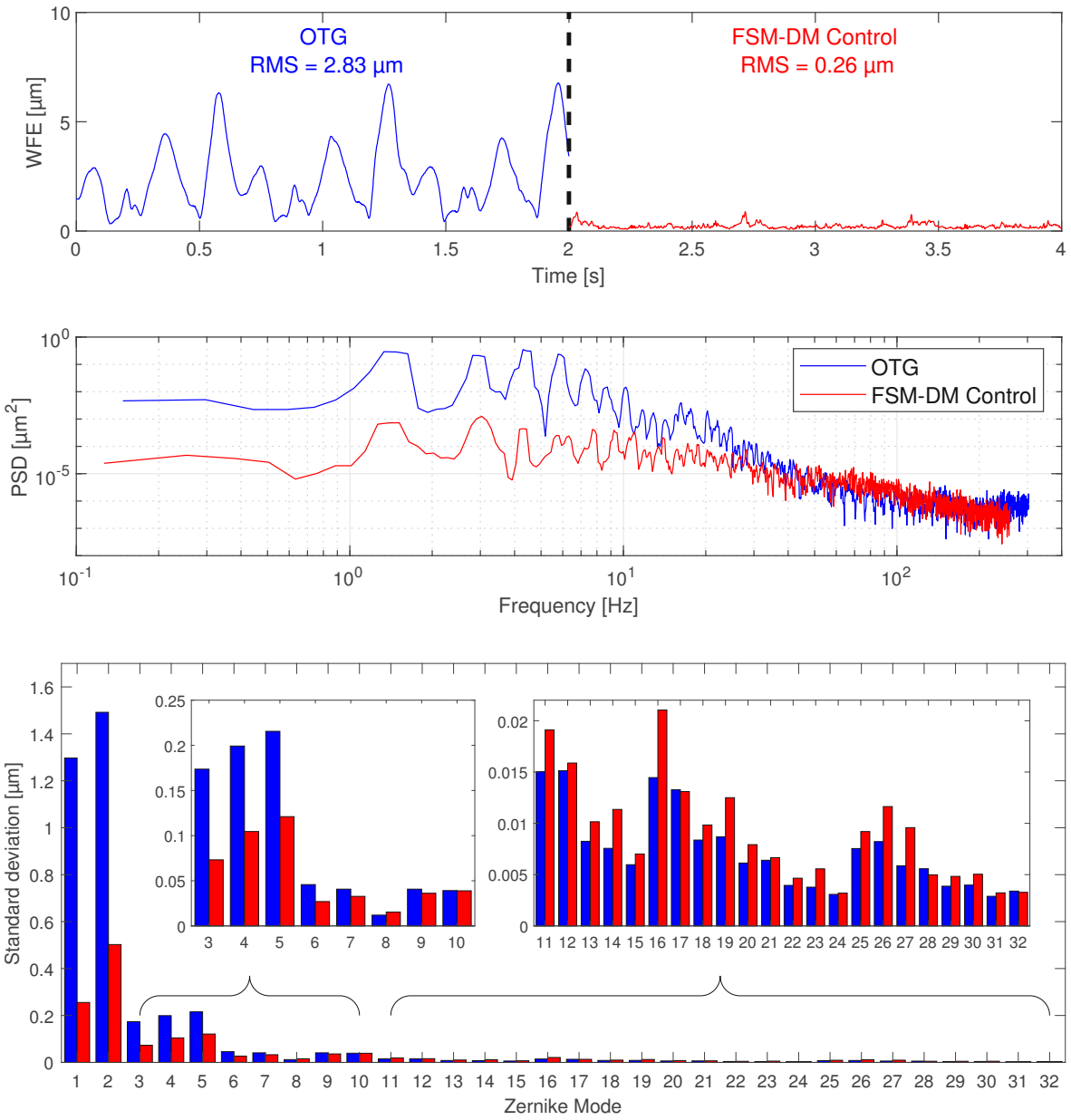

Modes	1-32	1	2	3	4	5	6	7	8-32
Ratio	23.8 %	9.4 %	8.6 %	44.5 %	55.6 %	53.6 %	60.3 %	75.6 %	107.4%

Figure 6.5: WFS measurements before and after activation of FSM and DM control. From top to bottom: RMS wavefront error over time, spectra of RMS wavefront error, STD of Zernike coefficients, Value changes of STD of Zernike coefficients.

The FSM-DM control can also be achieved by a modal separation of the two compensation controls. In this case, FSM control is compensating tip-tilt modes and DM control is compensating only the higher order modes without tip-tilt. Therefore, the compensation is independent of each other and any form of interaction between the two controls is prevented. This approach makes particular sense when the tip-tilt compensation

unburdens the DM from large strokes, increasing the bandwidth. The DM control uses a slope based feedback control and two strategies are tested to eliminate the tip-tilt compensation of this control. First by subtracting the gradient tip-tilt from the slope error, which is equivalent to subtracting the mean value and second by subtracting the Zernike tip-tilt, which is equivalent to subtracting a plane fit of the wavefront that corresponds to the Zernike coefficient 1 and 2. The subtraction of Zernike tip-tilt results in an unstable feedback control loop. The resulting fitting error is too high, which leads to unstable tip/tilt adjustments and therefore, this implementation can not be used. The subtraction of the gradient tip-tilt reaches a stable WFE after around 9 seconds (Figure 6.6). The cause of this slow drift behavior could not be determined but is potentially attributed to single spots on the WFS drifting out of their measurement range. The stationary part of the WFE shows a similar standard deviation as the FSM-DM control, however at an increased mean value. This could be caused by the uncompensated fraction of tip-tilt measured by the WFS, which is subtracted but not forwarded to the FSM.

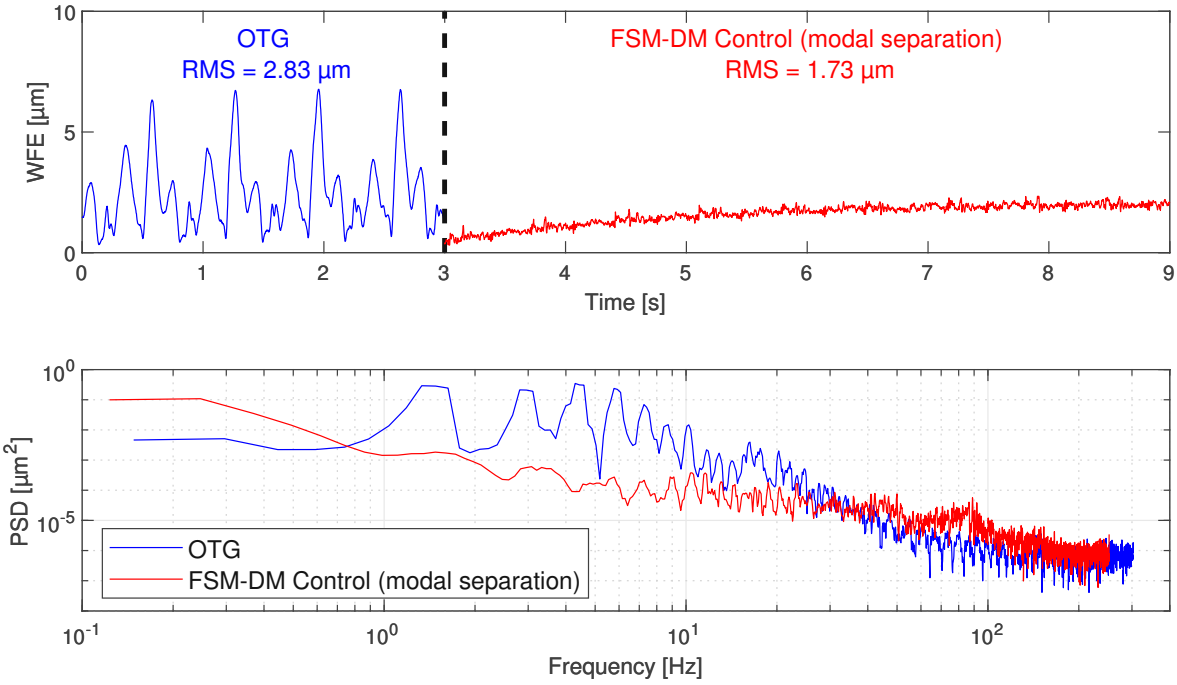

Figure 6.6: WFS measurements before and after activation of QPD/FSM and WFS/DM without gradient tilt control. (top) RMS wavefront error over time, (bottom) spectra of RMS wavefront error

The camera provides an additional tool to evaluate the different controls. The focused light beam creates a spot on the camera sensor and an image can be taken. By averaging the images over time the resulting long-exposure image is created. In case of a diffraction limited system this image should show the airy disk. In Figure 6.7 the time signal of the total wavefront error combined with averaged images consisting of 300 separate images are shown. With more advanced controls and therefore a reduction in total wavefront error the spot of the averaged image gets smaller. The improvement is clearly visible, but the airy disk does not appear, which indicates a non diffraction limited

system.

The WFS results of the different control combinations are combined in Figure 6.8. The table summarizes all exact drops of STD by Zernike modes in relation to no control activated. The Figure underlines that the FSM-DM control in series performs best.

Table 6.1 summarizes the drops in wavefront error by different number of compensated modes. By taking all modes from 1-32 into account the wavefront error drops by 76.2 %. Without tip-tilt, which is the sum of modes 3-32, the error drops by 7.9 %. Above mode 5 there is an insignificant change in wavefront error. Therefore, by taking these values into relation, tip-tilt compensation accounts for 89.6 % of the total wavefront error, modes 3-5 for 10.4 % and the compensation of modes above 5 are insignificant for the total wavefront error.

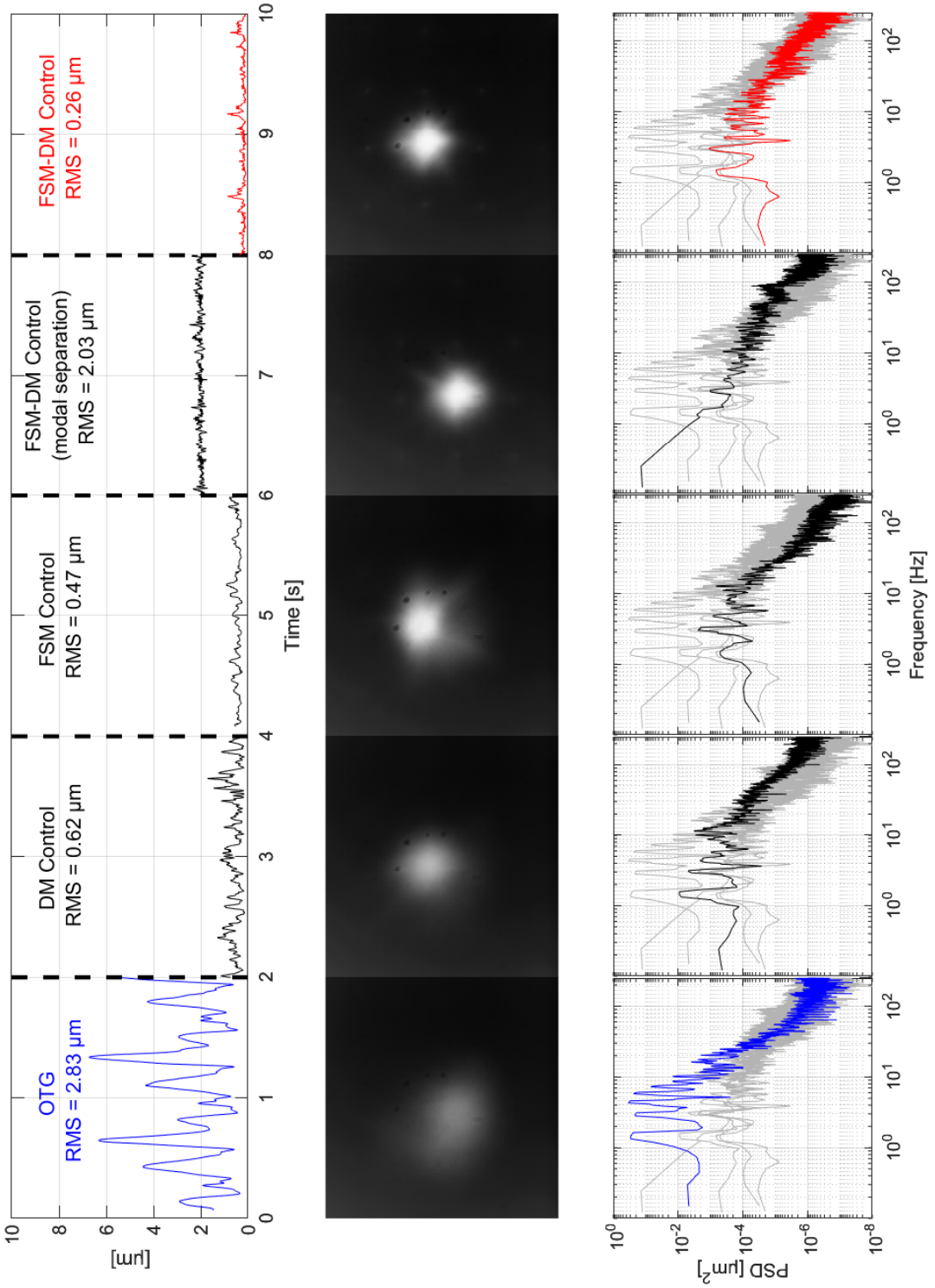

Figure 6.7: Comparison of all controls approaches by total RMS wavefront error over time, averaged images and spectrum of total RMS wavefront error.

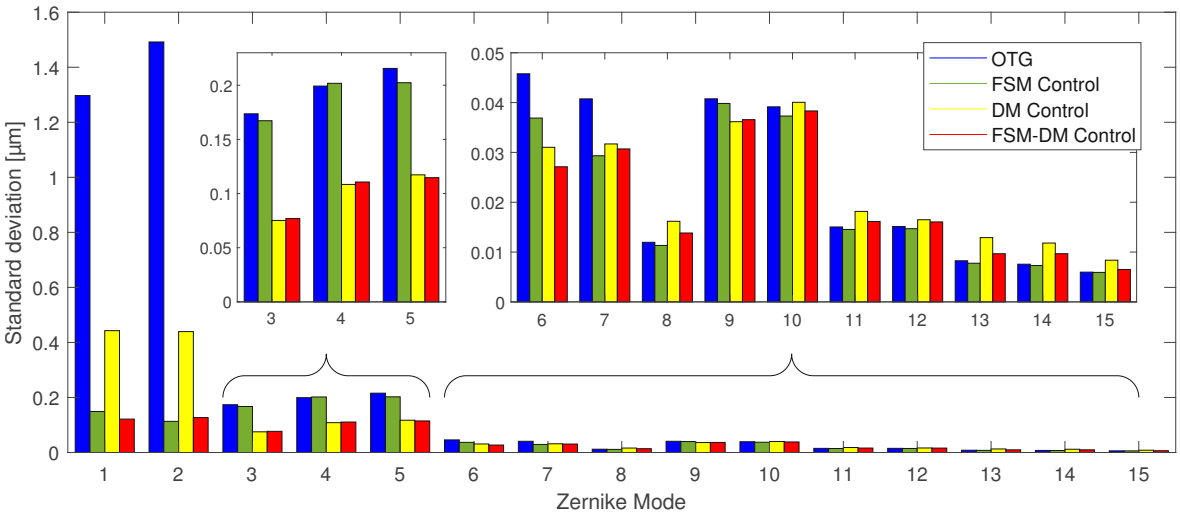

Modes	1-32	1	2	3	4	5	6	7	8-32
FSM control	30.5%	11.4%	7.6%	96.4%	100.2%	93.1%	79.7%	71.5%	95%
DM control	41.9 %	33.5 %	28.9 %	42.8 %	54.3 %	54.1 %	67.7 %	77.6 %	130%
FSM-DM control	23.8 %	9.4 %	8.6 %	44.5 %	55.6 %	53.6 %	60.3 %	75.6 %	107.4%

Figure 6.8: Comparison of different controls by STD of Zernike coefficients.

Table 6.1: Wavefront error drop by different number of compensated modes.

Compensated modes	1-32	2-32	3-32	4-32	5-32	6-32	7-32
Wavefront error	-76.2%	-44.6%	-7.9%	-5.3%	-2.9%	-0.25%	0.24%

In summary, all different control strategies lead to a reduced total wavefront error. The best result is achieved by the FSM-DM control in a reduction factor of 10.88. The FSM control achieves an improvement of 6.02 and the DM control of 4.56. The resulting images of the camera approach a distinct point. The compensation of tip-tilt accounts for 89.6 % of the total wavefront error reduction, modes 3-5 for 10.4 % and higher order modes are insignificant.

CHAPTER 7

Conclusion and Outlook

Small telescope systems enable cost-efficient, robust solution for a wide range of applications. However, atmospheric turbulence, tracking errors and vibrations introduce optical aberrations and thus, limit the achievable performance. An adaptive optics (AO) system allows the compensation of these optical aberrations. AO systems are highly complex and therefore hardly used in small telescope systems so far. Nevertheless, they can significantly increase the performance of such systems.

In this thesis the various compensation strategies of an AO system for a small telescope are evaluated. Goal is to characterize the trade-off between system complexity and remaining wavefront error and to evaluate the interaction between tip-tilt and higher order compensation. The system consists of a fast tip-tilt compensation system using a combination of a QPD and FSM (FSM control), with an implemented PID controller and a higher order mode compensation system implemented with a WFS and a DM (DM control), with an Integral controller. The setup is tested with a custom-made optical turbulence generator which implements a typical disturbance spectrum recorded using the LEO object SL16RB.

The implemented feedback loops have a -3 dB crossover frequency of the sensitivity functions of 335 and 330 Hz for FSM control and 13.5 Hz for DM control. Several control combinations are implemented and tested with the optical turbulence generator. All implemented control strategies reduce the total wavefront RMS error. By activating the DM control the total wavefront RMS error is reduced by a factor of 4.56. With the tip-tilt compensation of FSM control the resulting factor is 6.02. Both controls combined in series(FSM-DM control) result in a wavefront error reduction by a factor of 10.88, successfully demonstrating the potential of the developed approach.

> Research Question 1: How does the trade-off between correction performance and number of compensated modes affect the overall system's performance?

The trade-off can be answered with Figure 6.7, which shows the percentage of the compensated total wavefront error by different sum of modes. 76.2% of the total wavefront error is compensated with of all modes. With tip-tilt removed the reduction is lowered to 7.9%. With modes higher than 5 no significant reduction is achieved. Therefore, the tip-tilt aberrations account for 89.6% of the total wavefront error reduction. The modes 3 to 5 account for the remaining 10.4 % error of the total reduction. Additional compensation of higher order modes provides no benefit for the given disturbance and system implementation.

> Research Question 2: Is the dynamic behaviour of the deformable mirror observed at the wavefront sensor and therefore needs to be considered in the control system design?

No, with the used components the deformable mirrors' suspension mode is located around 1.3 kHz while the WFS is running at a sampling rate of 650 Hz. The measured time delay between actuation command and measuring the actuation is 4 ms, which results in - 180° phase value at 125 Hz (Figure 4.8). Therefore, the dynamic behavior is not apparent at the wavefront sensor and does not need to be considered. However, if the sampling rate is significantly increased the dynamic can get apparent.

> Research Question 3: How does the tip-tilt compensation affect higher-order aberrations and their compensation?

The tip-tilt compensation positively affects higher-order aberrations. The activation of FSM control alone leads to reduced higher order aberrations (Figure 6.7). The results in the upper table show, that the contribution of the higher order modes 3,5,6,7 are reduced by 96.4%, 93.1%, 79.7%, 71.5% respectively and orders from 8-32 to 95%. By additionally compensating tip-tilt aberrations with FSM control in series to the DM control, improvements in modes 6,7 and the sum of 8-32 are observable. Modes 3 to 5 remain in the same range with some decline up to 1.7 %. Consequently, it can be deducted that the tip-tilt compensation by FSM control alone leads to a slight decrease in higher order aberrations. In case of activating it in addition to the DM control, it leads to a slight decrease in modes greater than 5.

> Research Question 4: Is it possible to sepearate the controller design of tip-tilt compensation and higher order compensation?

Yes, the separation in the implemented AO system is achieved by the different bandwidths of the controls and the optical design, that splits up the compensation of QPD/FSM and WFS/DM. This results in a cascaded compensation with the FSM control being the faster inner loop with a bandwidth of 330 Hz and the DM control being the slower outer loop with a bandwidth of 13.5 Hz. The advantage of this design is the modularity, because the components and control approaches can easily be

changed as long as the difference in bandwidths is sufficient. This allows to optionally add/use a higher order AO system without changing the tip-tilt compensation loop. The disadvantage is that the beam at the QPD is not compensated in higher order modes, which may reduce the performance under strong turbulence. Another method is the modal separation of both controls, which splits up the compensation so that tip-tilt is only compensated with the FSM control and higher order modes are compensated with the DM control. The advantage is that the QPD can now be placed after the DM without any unintended interaction of the two control systems.

Outlook

Further improvements or research of the current system can be done by:

- Combining the control system by integrating both controls on one platform. For that the WFS and Deformable mirror needs a custom control and access. As a result the optical design and controller design can be adjusted to many mores sophisticated designs.
- Further testing and optimizing the optical turbulence generator. Additionally, trying out new methods of optical turbulence generators in the setup like hot air.
- Testing the adaptive optics on a telescope and a free-space link to gain further information of the performance of the system.

Bibliography

[1] M. Cegarra Polo and A. Lambert. Towards a Network of Small Aperture Telescopes with Adaptive Optics Correction Capability. In Sandy Ryan, editor, *Advanced Maui Optical and Space Surveillance Technologies Conference*, page 65, September 2016.

[2] M. Quintavalla, J. Mocci, R. Muradore, A. J. Corso, and S. Bonora. Adaptive optics on small astronomical telescope with multi-actuator adaptive lens. In Hamid Hemmati and Don M. Boroson, editors, *Free-Space Laser Communication and Atmospheric Propagation XXX*, volume 10524, page 1052414. International Society for Optics and Photonics, SPIE, 2018.

[3] Yujiro Sugino, Masahiro Ikenaga, and Daisuke Mizuno. Optimization of optical trapping and laser interferometry in biological cells. *Applied Sciences*, 10(14), 2020.

[4] H. W. Babcock. The possibility of compensating astronomical seeing. *Publications of the Astronomical Society of the Pacific*, 65(386):229, oct 1953.

[5] Mikhail Loktev, Gleb Vdovin, and Oleg Soloviev. Integrated adaptive optics system for small telescopes. *Proceedings of SPIE, 2008 vol. 7015*, 7015, 07 2008.

[6] Manuel Cegarra and Andrew Lambert. Low cost adaptive optics testbed for small telescopes. In *Proceedings of the International Conference on Photonics, Optics and Laser Technology - Volume 1: PHOTOPTICS*, pages 45–51. INSTICC, SciTePress, 2013.

[7] Copyright. In Robert K. Tyson, editor, *Principles of Adaptive Optics*, page iv. Academic Press, 1991.

[8] Robert J. Noll. Zernike polynomials and atmospheric turbulence∗. *J. Opt. Soc. Am.*, 66(3):207–211, Mar 1976.

[9] Wenjin Liu, Lizhi Dong, Ping Yang, Xiang Lei, Hu Yan, and Bing Xu. A zernike

mode decomposition decoupling control algorithm for dual deformable mirrors adaptive optics system. *Optics express*, 21:23885–23895, 10 2013.

[10] Glenn A. Tyler. Bandwidth considerations for tracking through turbulence. *J. Opt. Soc. Am. A*, 11(1):358–367, Jan 1994.

[11] F. Dow (ed.) Shack, R.V. (1971). Smith. Production and use of a lenticular hartmann screen. *Journal of the Optical Society of America (Oral presentation). Ramada Inn, Tucson, Arizona. 61*, 1971.

[12] Pierre Kern, Pierre Lena, Pierre Gigan, Jean-Claude Fontanella, Gerard Rousset, Fritz Merkle, and Jean-Paul Gaffard. Come-On: An Adaptive Optics Prototype Dedicated To Infrared Astronomy. In Jean-Pierre Swings, editor, *New Technologies for Astronomy*, volume 1130, pages 17 – 28. International Society for Optics and Photonics, SPIE, 1989.

[13] Simone Esposito, Armando Riccardi, Enrico Pinna, Alfio Puglisi, Fernando Quiros Pacheco, Carmelo Arcidiacono, Marco Xompero, Runa Briguglio, Guido Agapito, Lorenzo Busoni, Luca Fini, Javier Argomedo, Alessandro Gherardi, Guido Brusa, Douglas Miller, Juan Guerra, Paolo Stefanini, and Piero Salinari. Large binocular telescope adaptive optics system: New achievements and perspectives in adaptive optics. *Proc SPIE*, 8149, 03 2012.

[14] Marcos A. van Dam, David Le Mignant, and Bruce A. Macintosh. Performance of the keck observatory adaptive-optics system. *Appl. Opt.*, 43(29):5458–5467, Oct 2004.

[15] Olivier Guyon, Yutaka Hayano, Motohide Tamura, Tomoyuki Kudo, Shin Oya, Yosuke Minowa, Olivier Lai, Nemanja Jovanovic, Naruhisa Takato, Jeremy Kasdin, Tyler Groff, Masahiko Hayashi, Nobuo Arimoto, Hideki Takami, Colin Bradley, Hajime Sugai, Guy Perrin, Peter Tuthill, and Ben Mazin. Adaptive optics at the Subaru telescope: current capabilities and development. In Enrico Marchetti, Laird M. Close, and Jean-Pierre Véran, editors, *Adaptive Optics Systems IV*, volume 9148, page 91481R. International Society for Optics and Photonics, SPIE, 2014.

[16] Andreas Sinn, Thomas Riel, Peter Kremsner, and Georg Schitter. Analysis of tip-tilt compensation for reflective free-space optical satellite communication. In Hamid Hemmati and Don M. Boroson, editors, *Free-Space Laser Communications XXXI*, volume 10910, page 109101G. International Society for Optics and Photonics, SPIE, 2019.

[17] Andreas Sinn, Thomas Riel, Florian Deisl, Stephan Schachner, and Georg Schitter. High-bandwidth tip-tilt vibration compensation in telescope systems. *IFAC-PapersOnLine*, 52(15):549–554, 2019. 8th IFAC Symposium on Mechatronic Systems MECHATRONICS 2019.

[18] F.Yu. Kanev and V.P. Lukin. Towards a Network of Small Aperture Telescopes with Adaptive Optics Correction Capability. In *878 Atmos. Oceanic Opt. Vol. 4, No. 12*, December 1991.

[19] Shijie Hu, Bing Xu, Xuejun Zhang, Jing Hou, Jian Wu, and Wenhan Jiang. Double-deformable-mirror adaptive optics system for phase compensation. *Appl. Opt.*, 45(12):2638–2642, Apr 2006.

[20] R. Conan, C. Bradley, P. Hampton, O. Keskin, A. Hilton, and C. Blain. Distributed modal command for a two-deformable-mirror adaptive optics system. *Appl. Opt.*, 46(20):4329–4340, Jul 2007.

[21] Donald Gavel and Andrew Norton. Woofer-tweeter deformable mirror control for closed-loop adaptive optics: Theory and practice. *Proceedings of SPIE - The International Society for Optical Engineering*, 9148, 07 2014.

[22] Peter Hampton, Rodolphe Conan, Colin Bradley, and Panajotis Agathoklis. Control of a woofer tweeter system of deformable mirrors - art. no. 62741z. *Proceedings of SPIE - The International Society for Optical Engineering*, 07 2006.

[23] Kate Jackson, Rodolphe Conan, and Jean-Pierre Veran. Experimental validation of type-II tip-tilt control in a woofer-tweeter adaptive optics system. In Brent L. Ellerbroek, Michael Hart, Norbert Hubin, and Peter L. Wizinowich, editors, *Adaptive Optics Systems II*, volume 7736, page 77364K. SPIE, 2010.

[24] Tao Cheng, ZhenXin Xu, Kangjian Yang, Shuai Wang, Xin He, Ping Yang, and Bin Xu. A decoupling control algorithm for woofer-tweeter adaptive optics system in generalized irregular pupil region. *Optics Communications*, 472:125856, 2020.

[25] R. Conan, C. Bradley, P. Hampton, O. Keskin, A. Hilton, and C. Blain. Distributed modal command for a two-deformable-mirror adaptive optics system. *Appl. Opt.*, 46(20):4329–4340, Jul 2007.

[26] Shijie Hu, Bing Xu, Xuejun Zhang, Jing Hou, Jian Wu, and Wenhan Jiang. Double-deformable-mirror adaptive optics system for phase compensation. *Appl. Opt.*, 45(12):2638–2642, Apr 2006.

[27] Wenjin Liu, Lizhi Dong, Ping Yang, Xiang Lei, Hu Yan, and Bing Xu. A zernike mode decomposition decoupling control algorithm for dual deformable mirrors adaptive optics system. *Opt. Express*, 21(20):23885–23895, Oct 2013.

[28] Jean-François Lavigne and Jean-Pierre Véran. Woofer-tweeter control in an adaptive optics system using a fourier reconstructor. *J. Opt. Soc. Am. A*, 25(9):2271–2279, Sep 2008.

[29] Peter J. Hampton, Pan Agathoklis, Rodolphe Conan, and Colin Bradley. Closed-loop control of a woofer–tweeter adaptive optics system using wavelet-based phase reconstruction. *J. Opt. Soc. Am. A*, 27(11):A145–A156, Nov 2010.

[30] Weiyao Zou, Xiaofeng Qi, and Stephen A. Burns. Wavefront-aberration sorting and correction for a dual-deformable-mirror adaptive-optics system. *Opt. Lett.*, 33(22):2602–2604, Nov 2008.

[31] Stephen A. Burns Weiyao Zou, Xiaofeng Qi. Woofer-tweeter adaptive optics scanning laser ophthalmoscopic imaging based on lagrange-multiplier damped least-squares algorithm. *Biomed. Opt. Express*, 2(7):1986–2004, Jul 2011.

[32] Weiyao Zou and Stephen A. Burns. Testing of lagrange multiplier damped least-squares control algorithm for woofer-tweeter adaptive optics. *Appl. Opt.*, 51(9):1198–1208, Mar 2012.

[33] Chaohong Li, Nripun Sredar, Kevin M. Ivers, Hope Queener, and Jason Porter. A correction algorithm to simultaneously control dual deformable mirrors in a woofer-tweeter adaptive optics system. *Opt. Express*, 18(16):16671–16684, Aug 2010.

[34] Tao Cheng, Wenjin Liu, Boqing Pang, Ping Yang, and Bing Xu. A slope-based decoupling algorithm to simultaneously control dual deformable mirrors in a woofer-tweeter adaptive optics system*. *Chinese Physics B*, 27(7):070704, jul 2018.

[35] Tao Cheng, WenJin Liu, KangJian Yang, Xin He, Ping Yang, and Bing Xu. Testing for a slope-based decoupling algorithm in a woofer-tweeter adaptive optics system. *Appl. Opt.*, 57(13):3357–3364, May 2018.

[36] Jan van Eijk Robert Munnig Schmidt, Georg Schitter. *The Design of High Performance Mechatronics*. IOS Press under the imprint Delft University Press, 2011.

[37] H. Campbell and A.H. Greenaway. Wavefront sensing: From historical roots to the state-of-the-art. *EAS Publications Series*, 22:165 – 185, 01 2006.

[38] Ernst Csencsics and Georg Schitter. Exploring the pareto fronts of actuation technologies for high performance mechatronic systems. *IEEE/ASME Transactions on Mechatronics*, PP:1–1, 08 2020.

[39] Christopher C. Wilcox, Jonathan R. Andrews, Sergio R. Restaino, Scott W. Teare, Don M. Payne, and Sanjay Krishna. Analysis of a combined tip-tilt and deformable mirror. *Opt. Lett.*, 31(6):679–681, Mar 2006.

[40] Pierre-Yves Madec. Overview of deformable mirror technologies for adaptive optics and astronomy. *Proceedings of SPIE - The International Society for Optical Engineering*, 8447:05–, 07 2012.

[41] Alpao. *ALPAO-Deformable-Mirrors-datasheet*, 11 2023.

[42] John W. Hardy. *Adaptive Optics for Astronomical Telescopes*. Oxford University Press, 1998.

[43] D. P. Greenwood. Bandwidth specification for adaptive optics systems. *Journal of the Optical Society of America (1917-1983)*, 67:390–393, March 1977.

[44] Andreas Sinn, Christian Schwaer, Peter Kremsner, and Georg Schitter. High-bandwidth tip-tilt compensation for small telescope systems. In Laura Schreiber, Dirk Schmidt, and Elise Vernet, editors, *Adaptive Optics Systems VIII*, volume 12185 of *Society of Photo-Optical Instrumentation Engineers (SPIE) Conference Series*, page 1218584, August 2022.

[45] D. L. Fried. Optical resolution through a randomly inhomogeneous medium for very long and very short exposures. *J. Opt. Soc. Am.*, 56(10):1372–1379, Oct 1966.

[46] K. Strehl. Über luftschlieren und zonenfehler,. *Zeitschrift für Instrumentenkunde*, (22):213–217, 1902.

[47] Lewis Jr, Marshall Perrin, Franck Marchis, Anand Sivaramakrishnan, Russell Makidon, Julian Christou, Bruce Macintosh, Lisa Poyneer, Marcos van Dam, and Mitchell Troy. Is that really your strehl ratio? *Advancements in Adaptive Optics*, 5490, 10 2004.

[48] Pierre Y. Bely. *The Design and Construction of Large Optical Telescopes*. Springer-Verlag New York, Inc., 2003.

[49] Laurent Jolissaint. Optical turbulence generators for testing astronomical adaptive optics systems: A review and designer guide. *Publications of the Astronomical Society of the Pacific*, 118:0–0, 10 2006.

[50] Troy A. Rhoadarmer and J. Roger P. Angel. Low-cost, broadband static phase plate for generating atmosphericlike turbulence. *Appl. Opt.*, 40(18):2946–2955, Jun 2001.

[51] Ji Yong Joo, Seok Gi Han, Jun Ho Lee, Hyug-Gyo Rhee, Joon Huh, Kihun Lee, and Sang Yeong Park. Development and characterization of an atmospheric turbulence simulator using two rotating phase plates. *Curr. Opt. Photon.*, 6(5):445–452, Oct 2022.

[52] Sandrine Thomas. A simple turbulence simulator for adaptive optics. In Domenico Bonaccini Calia, Brent L. Ellerbroek, and Roberto Ragazzoni, editors, *Advancements in Adaptive Optics*, volume 5490, pages 766 – 773. International Society for Optics and Photonics, SPIE, 2004.

[53] Christopher Wilcox, Jonathan Andrews, Sergio Restaino, Ty Martinez, and Scott Teare. Atmospheric turbulence generator using a liquid crystal spatial light modulator. *IEEE Aerospace Conference Proceedings*, pages 1–8, 03 2007.

[54] Onur Keskin, Laurent Jolissaint, and Colin Bradley. Hot-air optical turbulence generator for the testing of adaptive optics systems: Principles and characterization. *Applied optics*, 45:4888–97, 08 2006.

[55] Ernst Csencsics and Georg Schitter. Parametric pid controller tuning for a fast steering mirror. In *2017 IEEE Conference on Control Technology and Applications (CCTA)*, pages 1673–1678, 2017.